



國立臺灣大學電機資訊學院光電工程學研究所

碩士論文

Graduate Institute of Photonics and Optoelectronics
College of Electrical Engineering and Computer Science
National Taiwan University

Master Thesis

免用微影技術製作的氮化鎵奈米光柵結構內量子點發光、福
斯特共振能量轉移與表面電漿子耦合隨偏振變化的行為
Polarization-dependent Behaviors of Quantum-dot Emission,
Förster Resonance Energy Transfer, Surface Plasmon Coupling in
Lithography-free GaN Nano-grating Structures

馮璽宇

Hsi-Yu Feng

指導教授：楊志忠 博士

Advisor: Chih-Chung Yang, Ph.D.

中華民國 112 年 10 月

October 2023

口試委員審定書

國立臺灣大學碩士學位論文 口試委員會審定書

MASTER'S THESIS ACCEPTANCE CERTIFICATE
NATIONAL TAIWAN UNIVERSITY

免用微影技術製作的氮化鎵奈米光柵結構內量子點發
光、福斯特共振能量轉移與表面電漿子耦合隨偏振變化
的行為

Polarization-dependent Behaviors of Quantum-dot
Emission, Förster Resonance Energy Transfer, Surface
Plasmon Coupling in Lithography-free GaN Nano-grating
Structures

本論文係馮璽宇君（學號 R09941099）在國立臺灣大學光電工程學研
究所完成之碩士學位論文，於民國 112 年 10 月 5 日承下列考試委員審
查通過及口試及格，特此證明。

The undersigned, appointed by the Graduate Institute of Photonics and Optoelectronics, on 5 October
2023 have examined a Master's thesis entitled above presented by FENG, HSI-YU (student ID:
R09941099) candidate and hereby certify that it is worthy of acceptance.

口試委員 Oral examination committee:

(指導教授 Advisor)

楊志忠

廖哲浩

吳育任

黃建璋

林建中

所長 Director:

吳育任

誌謝



首先感謝指導教授楊志忠博士三年的指導與鼓勵，引領我進入光電工程的研究領域。每一次會議、每一封郵件以及每一句指導，都可以看到老師對學生的用心，老師不吝嗇地傳授我其一生的經驗，從待人處事到科學研究，無一不受用無窮，雖然如今的我在科研的道路上只能算是初出茅廬的毛頭小子，但我相信經過老師這三年的砥礪，我能因此走的更穩健更遙遠，在此致上我最深的感謝。

其次要感謝台大光電所的同学，在實驗上給予我的建議以及與討論，讓我可以順利地完成這篇論文。

接著感謝楊少波學長在氮化鎵樣品的提拱，陳威呈同學在 TEM 量測的協助，林育聖同學、黃慶豪學弟在光學量測分析方面的幫忙，以及浚瑞、岳錡、力平在研究生活中相互的鼓勵。

最後要感謝我的家人，他們在生活上對我的關切、支持，以及在我身後給我鼓勵，使得我在求學過程中更加順利，終能順利地完成碩士學位。謹以此文獻給我的父母及家人。

璽宇 謹誌於台大 2023 年 10 月

摘要

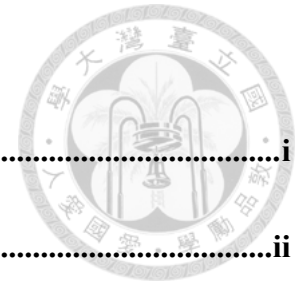


我們設計氮化鎵磊晶結構和長條形台階陣列，經由電化學蝕刻可在整片樣品上製成次表面定向的孔洞結構。在去除氮化鎵覆蓋層後，我們可獲得台狀上具有固定延伸方向的表面週期性溝槽，這就實現了不必使用任何奈米微影製程，卻可得到週期小於 100 奈米的深度光柵。我們利用滴塗方法可將膠體量子點和化學合成的銀奈米顆粒塞入溝槽內，以此來展現其隨偏振變化的光學特性。基於穿透、連續光致發螢光和時間分辨光致發螢光測量，我們研究隨偏振變化的表面電漿子共振及耦合、福斯特共振能量轉移和量子點發光行為。當激發偏振垂直於溝槽方向時，量子點發光和表面電漿子耦合增強，然而福斯特共振能量轉移效率降低。當激發偏振垂直於溝槽方向時，整體光色轉換效率較高。

Abstract

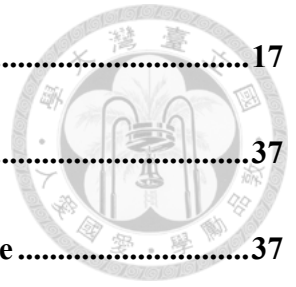
Subsurface oriented pores in a GaN layer are first formed through an electrochemical etching process by carefully designing the epitaxial structure and the geometry of a stripe mesa array. The, after removing a GaN capping layer, surface oriented trenches of a fixed extension direction on the mesas are implemented to achieve a deep grating of sub-100 nm in period without using any nano-lithography process. By drop-casting colloidal quantum dots (QDs) and chemically synthesized Ag nanoparticles (NPs) onto the surface of such a sample, they can settle into the trenches for showing their polarization-dependent optical properties. Polarization-dependent surface plasmon (SP) resonance and coupling, Förster resonance energy transfer (FRET), and QD emission are studied based on the measurements of transmission, continuous photoluminescence (PL) and time-resolved PL spectroscopies. When the excitation polarization is perpendicular to the trench orientation, QD emission and SP coupling are stronger. However, the FRET efficiency is lower. The overall color conversion efficiency is higher when the excitation polarization is perpendicular to the trench orientation.

Content



| | |
|---|-----------|
| 口試委員審定書 | i |
| 誌謝..... | ii |
| 摘要..... | iii |
| Abstract..... | iv |
| Content: | v |
| List of Figure: | vii |
| List of Table | xi |
| Chapter 1 Introduction..... | 1 |
| 1.1 Nanoscale-cavity effects..... | 1 |
| 1.2 Subsurface GaN porous structures | 3 |
| 1.3 Behaviors of quantum dot emission and Förster resonance energy transfer in a subsurface GaN porous structure | 4 |
| 1.4 Research motivations | 6 |
| 1.5 These structure..... | 6 |
| Chapter 2 Sample Structures, Fabrication Procedures, and Measurement Methods . . | 12 |
| 2.1 Epitaxial structure | 12 |
| 2.2 Fabrications of mesa and porous structures..... | 12 |
| 2.3 Sample designations and structures | 15 |

| | |
|--|-----------|
| 2.4 Optical measurements | 17 |
| Chapter 3 Polarization Dependent Optical Measurement Results | 37 |
| 3.1 Polarization dependent localized surface plasmon resonance | 37 |
| 3.2 Polarization dependent time-resolved photoluminescence of quantum dots | 38 |
| 3.3 Polarization dependent continuous photoluminescence measurement..... | 42 |
| Chapter 4 Discussions..... | 64 |
| 4.1 Polarization dependent surface plasmon resonance | 64 |
| 4.2 Polarization dependent quantum dot emission behaviors | 64 |
| 4.3 Accuracy of optical measurement..... | 65 |
| Chapter 5 Conclusions..... | 66 |
| References:..... | 67 |



List of Figure



| | |
|--|----|
| Fig 1.1 Structures of the four sample groups. | 10 |
| Fig 1.2 TEM and EDX images of a PS with inserted QDs. | 11 |
| Fig 2.1 Schematic illustration for the epitaxial structure used for sample fabrication, which is designated as epitaxial structure Po-XX. | 19 |
| Fig 2.2 Layout of the periodic pattern of stripe mesa. | 20 |
| Fig 2.3 Setup for an ECE process. | 21 |
| Fig 2.4 Flow paths of applied electric current and electrolyte in an ECE process for etching the conduction layers in a mesa. | 22 |
| Fig 2.5 (a)-(e): Fabrication procedures of a sample, including photolithography to define mesa (a), ICPRIE to fabricate mesa (b), ECE to form PS (c), another ICPRIE process to expose the upper PS (d), and drop-casting the solutions of QDs and Ag NPs (e)..... | 23 |
| Fig 2.6 (a)-(c): Photographs under a microscope of a sample after mesa fabrication, after ECE, and after the second ICPRIE process for exposing the PS, respectively. (d) and (e): Photographs of the whole sample after mesa fabrication and after ECE, respectively. ... | 24 |
| Fig 2.7 (a): Photograph of a sample after the second ICPRIE process for exposing the PS. (b) and (c): SEM images in the regions roughly circled by the red and blue rectangles in part (a). (d): Magnified SEM image in the region circled by the green rectangle in part (c). | 25 |

| | |
|--|----|
| Fig 2.8 (a)-(d): SEM images of samples S-GQD, S-RQD, S-GNP, and S-RNP, respectively. | 26 |
| | |
| Fig 2.9 Normalized PL spectra of GQD and RQD, and the normalized extinction spectra of GNP and RNP in water. | 27 |
| Fig 2.10 (a) and (b): SEM images of samples S-GQD+GNP and S-RQD+RNP, respectively. | 28 |
| | |
| Fig 2.11 (a)-(c): SEM images of samples S-GQD+RQD, S-GQD+RQD+GNP, and S-GQD+RQD+RNP, respectively. | 29 |
| Fig 2.12 (a)-(d): SEM images of samples P-GQD, P-RQD, P-GNP, and P-RNP, respectively. | 30 |
| | |
| Fig 2.13 (a) and (b): SEM images of samples P-GQD+GNP and P-RQD+RNP, respectively. | 31 |
| | |
| Fig 2.14 (a)-(c): SEM images of samples P-GQD+RQD, P-GQD+RQD+GNP, and P-GQD+RQD+RNP, respectively. | 32 |
| Fig 2.15 Cross-sectional TEM image of sample P-GQD+RQD+RNP..... | 33 |
| Fig 2.16 (a): EDX mapping of a TEM image of sample P-GQD+RQD+RNP. (b)-(f): EDX mappings of elements Cd, Se, Ag, Zn, and S. | 34 |
| Fig 2.17 Setup for continuous PL measurement. | 35 |
| Fig 2.18 Setup for time-resolved PL measurement..... | 36 |

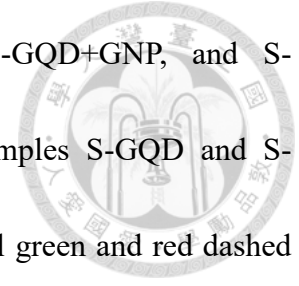


Fig 3.1 (a)-(c): Transmission spectra of samples S-GNP, S-GQD+GNP, and S-GQD+RQD+GNP, respectively, by using a GaN template, samples S-GQD and S-GQD+RQD as the normalization bases, respectively. The vertical green and red dashed lines indicate the emission peak wavelengths of GQD and RQD, respectively.....49

Fig 3.2 (a)-(c): Transmission spectra of samples S-RNP, S-RQD+RNP, and S-GQD+RQD+RNP, respectively, by using a GaN template, samples S-RQD and S-GQD+RQD as the normalization bases, respectively.....50

Fig 3.3 Transmission spectra of sample P-GNP under different polarization conditions, including the polarization directions tilted 0, 30, 60 and 90 degrees with respect to the PS trench orientation. The un-polarized transmission spectrum is also shown. The numbers after polarization angles in the labels show the transmission minimum wavelengths through Gaussian fitting.51

Fig 3.4 Results similar to those in Fig. 3.3 for sample P-GQD+GNP.....52

Fig 3.5 Results similar to those in Fig. 3.3 for sample P-GQD+RQD+GNP.....53

Fig 3.6 Results similar to those in Fig. 3.3 for sample P-RNP.....54

Fig 3.7 Results similar to those in Fig. 3.3 for sample P-RQD+RNP.55

Fig 3.8 Results similar to those in Fig. 3.3 for sample P-GQD+RQD+RNP.56

Fig 3.9 (a) and (b): Normalized PL decay profiles of the green and red components, respectively, for the surface samples.57

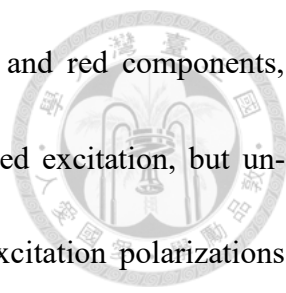


Fig 3.10 (a) and (b): Normalized PL decay profiles of the green and red components, respectively, for the PS samples under the conditions of polarized excitation, but unpolarized PL. The \perp and $//$ signs in the labels represent the excitation polarizations perpendicular to and parallel with the trench orientation.....58

Fig 3.11 (a) and (b): Normalized PL decay profiles of the green and red components, respectively, for part of the PS samples under the conditions of polarized excitation and polarized PL. In the labels, the first (second) sign describes the excitation (PL) polarization.....59

Fig 3.12 (a) and (b): Normalized PL decay profiles of the green and red components, respectively, for samples P-GQD+RQD+GNP and P-GQD+RQD+RNP under the conditions of polarized excitation and polarized PL.60

Fig 3.13 Normalized PL spectra of the three surface samples with both GQD and RQD. .61

Fig 3.14 (a) and (b): Normalized PL spectra of the PS samples when the excitation polarization is perpendicular to trench orientation under the conditions of unpolarized and polarized PL, respectively.....62

Fig 3.15 (a) and (b): Normalized PL spectra of the PS samples, similar to those in Figs. 3.14(a) and 3.14(b), respectively, when the excitation polarization is parallel with trench orientation.....63

List of Table

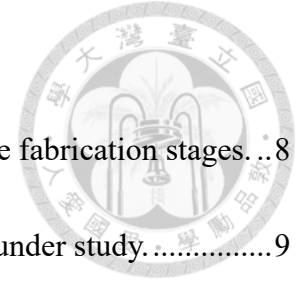


Table 1.1 QW PL decay times in the QW samples at different sample fabrication stages. ...8

Table 1.2 PL decay times of the green and red lights in the samples under study.9

Table 3.1 PL decay times of the green and red components in the surface samples. The numbers inside the parentheses show the PL decay rate enhancement percentages through SP coupling. The numbers inside the curly brackets show the FRET efficiencies.....45

Table 3.2 PL decay times of the green and red components in the PS samples under the conditions of polarized excitation, but un-polarized PL. The numbers inside the parentheses show the PL decay rate enhancement percentages through SP coupling. The numbers inside the curly brackets show the FRET efficiencies.....46

Table 3.3 PL decay times of the green and red components in the PS samples under the conditions of polarized excitation and polarized PL. The numbers before (after) the slashes show the PL decay times under the condition of \perp ($//$) PL polarization. The numbers inside the parentheses show the PL decay rate enhancement percentages through SP coupling. The numbers inside the curly brackets show the FRET efficiencies.....47

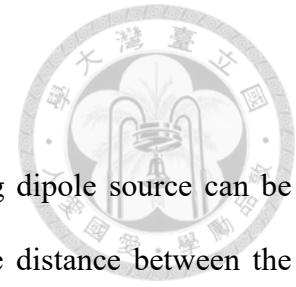
Table 3.4 R/G integrated intensity ratios in the surface and PS samples under various polarization combination conditions.48

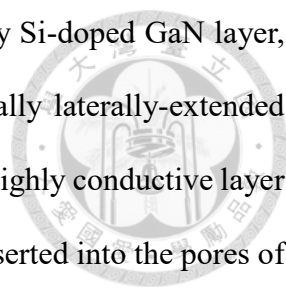
Chapter 1 Introduction

1.1 Nanoscale-cavity effects

The electromagnetic field generated by an infinitesimal radiating dipole source can be classified into the categories of far and near fields depending on the distance between the observation point and source position. Generally, near field distributes in the region within the distance of one-half the wavelength. Outside this region, far field dominates. From a radiating dipole source, the far field strength is proportional to the inverse of the distance. In the near field regime, more contributing terms inversely proportional to the higher powers of distance exist. Resonance modes in a cavity structure can be built with far field when its propagation distance in a round-trip is equal to an integral number of wavelength. The cavity resonance behavior is sensitive to cavity geometry. However, when the cavity dimension is smaller than one-half the wavelength, the near field distribution inside the cavity can produce certain effects on the radiation behavior of a dipole other than the aforementioned cavity resonance. On the other hand, the Purcell effect has been used for generally describing the influence of a cavity structure on the radiating dipole source inside the cavity [1]. The electromagnetic field distribution built at the dipole position produced by the scattering of the surrounding structure can change the radiation behavior of the dipole source and hence the overall radiation result. Either near or far field portion produced by a dipole source can lead to the Purcell effect for changing the near field distribution and far field radiated power.

With the development of nano-fabrication technique, nanoscale cavities of various geometries can be produced in light-emitting devices. The dimension of such a nanoscale cavity ranges from a couple tens through a few hundred nm. Light-emitting nanoparticles (NPs), such as colloidal quantum dots (QDs), can be inserted into such a nanoscale cavity. Such an inserted QD can produce a strong near field distribution inside such a cavity. The examples of nanoscale cavity for inserting QDs in a light-emitting device include a GaN porous structure and a surface





nano-hole. By growing a highly conductive GaN layer, such as a highly Si-doped GaN layer, in a GaN-based device, a subsurface GaN porous structure of essentially laterally-extended pores of several tens nm in cross-sectional size can be fabricated in the highly conductive layer through an electrochemical etching (ECE) process [2-6]. QDs can be inserted into the pores of such a porous structure for observing the enhanced QD emission efficiency, the stronger Förster resonance energy transfer (FRET) between the QDs of different emission wavelengths, and the stronger FRET from a nearby InGaN/GaN quantum well (QW) into the inserted QDs [7, 8]. Nanoscale cavities can also be implemented by fabricating surface nano-holes on a GaN template. Through nano-imprint lithography and reactive ion etching, a surface nano-hole array of a couple hundred nm in hole width and several hundred nm in hole depth can be obtained for filling with QDs and chemically synthesized metal NPs. Such a surface nano-hole structure has been used in a light-emitting device for enhancing the FRET from the embedded QWs into the filled-in QDs based on the advantageous short distance between the QWs and QDs [9-14]. As a matter of fact, a nano-hole structure can produce more advantageous results through the nanoscale-cavity effect, including a higher QD emission efficiency, a more effective FRET process, and a stronger surface plasmon (SP) coupling effect [15].

FRET and SP coupling are two important near-field interactions for enhancing light emission and color conversion. From the viewpoint of the electromagnetic theory, FRET is an absorption process of the near-field energy from an energy donor by an acceptor. Such an energy transfer is effective when the absorption spectrum of the acceptor overlaps the emission wavelength of the donor and the distance between the donor and acceptor is shorter than several tens nm [16-21]. FRET is a useful mechanism for color conversion, particularly when the energy donor and acceptor are placed inside or near a nanoscale cavity and hence their distance is small [7, 8, 16, 22]. The SP coupling between a light emitter and an SP resonance mode of a metal nanostructure can be understood as the process of energy transfer from the light emitter

into the SP resonance mode for radiation before the energy is consumed by the non-radiative process of the light emitter. Through SP radiation, the overall emission efficiency of the coupled system can be enhanced [23, 24]. For producing an effective SP coupling process, the distance between the light emitter and the metal nanostructure needs to be smaller than ~ 100 nm. Either deposited surface metal NPs or chemically synthesized metal NPs can be placed close to a QW or QD for inducing an effective SP coupling and hence a higher emission or FRET efficiency [20, 21, 25-29].

In a previous theoretical study in our laboratory, the electric field and radiated power of a radiating dipole located inside a spherical nano-cavity are formulated to show that the nano-cavity structure or nanoscale-cavity effect can enhance the near-field intensity inside the cavity and the far-field radiated power of the dipole. Such enhancements are caused by two contributing factors, including the classical electromagnetic scattering as formulated and the Purcell effect, which is implemented through a numerical feedback process by assuming a two-level system for the radiating dipole. The enhancement of near-field intensity results in the efficiency increase of FRET when both energy donor and acceptor are located inside the nano-cavity. By combining the enhancements of the field intensity of the donor and the radiated power of the acceptor, the color conversion efficiency can be increased through the nanoscale-cavity effect. We also numerically demonstrate that the nanoscale-cavity effect can enhance SP coupling for increasing the radiated power of a dipole located nearby an Ag NP inside a nano-cavity.

1.2 Subsurface GaN porous structures

GaN can be wet-etched by acids, such as HNO_3 , or alkalis, such as KOH. In ECE, we can use the flow path of electric current to control the etching structure for forming subsurface extended pores in GaN. Such essentially lateral pores in GaN can be fabricated by placing the

anode contact on an edge face of a GaN sample in an electrochemical system [2-6]. In such an etching process, certain surface holes can be formed on the top surface for the electrolyte to flow into the subsurface layer to be etched and for the gases produced in the chemical reactions to come out from the etched regions. In an ECE process, wet etching can occur in a highly conductive layer, such as a highly Si-doped n-type GaN layer, inside the GaN sample. Therefore, essentially lateral tube-like voids with a certain orientation can be formed inside a GaN sample. GaN and AlGaIn PSs have been used for increasing LED crystal quality and light extraction [30-34], lifting a GaN layer or an LED structure from substrate [35-37], forming a distributed Bragg reflector [38, 39], relaxing strain [33, 34, 40-42], embedding QDs in a vertical PS for display application [43], and fabricating lateral and vertical laser diodes [44-46].

1.3 Behaviors of quantum dot emission and Förster resonance energy transfer in a subsurface GaN porous structure [7]

To improve the color conversion performance, the nanoscale-cavity effects on the emission efficiency of a colloidal QD and the FRET from quantum well (QW) into QD in a GaN porous structure (PS) has been studied [7]. For this study, green-emitting QD (GQD) and red-emitting QD (RQD) are inserted into the fabricated PSs in a GaN template and a blue-emitting QW template, and investigate the behaviors of the photoluminescence (PL) decay times and the intensity ratios of blue, green, and red lights. In the PS samples fabricated on the GaN template, the efficiency enhancements of QD emission and the FRET from GQD into RQD, when compared with the samples of surface QDs, which is attributed to the nanoscale-cavity effect, are observed. In the PS samples fabricated on the QW template, the FRET from QW into QD is also enhanced. The enhanced FRET and QD emission efficiencies in a PS result in an improved color conversion performance. Because of the anisotropic PS in the sample surface

plane, the polarization dependencies of QD emission and FRET are observed. In Fig. 1.1, we illustrate the structures of four sample groups, including those with surface QDs on GaN and QW templates (sample designations with -S), and those with QDs inserted into subsurface PSs inside GaN and QW templates (sample designations with -H). Green- and red-emitting QDs (GQD and RQD, respectively) are used for inserting into PSs. In Fig. 1.2(a), we show the TEM image of a PS. In Fig. 1.2(b), an EDX image of the PS is shown, illustrating the distribution of QD composition elements and confirming the successful insertion of QDs into the PS. Table 1.1 shows the QW photoluminescence (PL) decay times in the QW samples at different sample fabrication stages. The numbers inside the parentheses show the corresponding FRET efficiencies. The numbers inside the curly brackets show the corresponding internal quantum efficiency (IQE) values. Because of the anisotropic pore structure, the measured optical properties in the polarizations along (//) and perpendicular (\perp) to the applied current direction are different. Here, one can see that after PS fabrication, the QW PL decay time is reduced and the corresponding IQE is increased. The FRET efficiency (eff.) is significantly increased when QDs are inserted into a PS, demonstrating the effect of the nanoscale cavity on enhancing the FRET and hence color conversion efficiencies.

In Table 1.2, we show the PL decay times of the green and red lights in various samples illustrated in Fig. 1.1, including the two polarizations when QDs are inserted into the PSs. Here, one can see that the QD PL decay time of either green or red light in a PS sample is always shorter than that of the corresponding surface sample, indicating the nanoscale-cavity effect for enhancing the QD emission efficiency. Also, the QD PL decay time of a sample fabricated on a QW template is always longer than that of the corresponding sample fabricated on a GaN template, indicating the effective FRET from QW into QD no matter QDs are located on the sample surface or inside a PS. Meanwhile, the PL decay time in the \perp -polarization is always shorter than that in the // -polarization, indicating the stronger QD emission and FRET from

QW into QD in the \perp -polarization. This result again confirms the importance of the nanoscale-cavity effect.



1.4 Research motivations

As illustrated in Fig. 1.2 and discussed in section 1.3, we have developed a technique to insert QDs into a PS for observing the enhanced QD emission and FRET efficiencies. However, it is still difficult to insert metal NPs into the pores of a PS. If metal NPs can be inserted into a PS, we can study the SP coupling behaviors in such a nanoscale cavity, i.e., the nanoscale-cavity effect on SP coupling. Also, if metal NPs can be inserted into a subsurface PS, they can be closer to a QW structure for inducing a stronger SP coupling effect. In particular, due to the anisotropic pore structure in a PS, polarization-dependent SP coupling behaviors are expected. This behavior is useful for producing polarized emission from a colloidal QD. Nevertheless, the insertion of metal NPs into a subsurface PS is difficult. For investigating the polarization-dependent nanoscale-cavity effect, in this study, we develop an ECE technique to fabricate almost parallel pores in a PS. After removing the capping layer of the PS, a surface nano-grating structure can be obtained. The grating period can range from several tens through a couple hundred nm. Such a surface nano-grating structure is obtained without using any lithography process, but simply well controlling the ECE condition. Then, by inserting QDs and Ag NPs into the grooves of the nano-grating, polarization-dependent QD emission, FRET, and SP coupling can be implemented. The polarization-dependent nanoscale-cavity effects can be well understood.

1.5 These structure

In Chapter 2 of this thesis, the used epitaxial structure, mesa pattern, sample structures, sample fabrication procedures, and optical measurement methods are described. The optical

measurement results, including transmission spectra, time-resolved photoluminescence (PL) behaviors, and continuous PL spectra, are demonstrated and analyzed in Chapter 3. Then, certain discussions about the experimental results are given in Chapter 4. Finally, conclusions are drawn in Chapter 5.

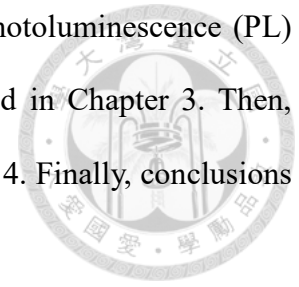
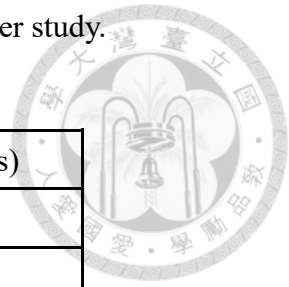


Table 1.1 QW PL decay times in the QW samples at different sample fabrication stages.

| sample | QW/GQD-S (ns) | QW/RQD-S (ns) | QW/GQD-P (ns) | QW/RQD-P (ns) |
|--------------------------------|----------------------------|----------------|----------------|----------------|
| Intrinsic | 6.04 {IQE = 44.0 %} | 5.78 {45.2 %} | 6.15 {44.2 %} | 6.19 {44.7 %} |
| after PS fabrication | --- | --- | 5.68 {54.2 %} | 5.54 {52.3 %} |
| after QD application | 5.12 (FRET eff. = 15.23 %) | 4.91 (15.05 %) | --- | --- |
| after QD insertion (//) | --- | --- | 3.62 (36.27 %) | 3.95 (28.70 %) |
| after QD insertion (\perp) | --- | --- | 3.59 (36.80 %) | 4.02 (27.44 %) |

Table 1.2 PL decay times of the green and red lights in the samples under study.



| Sample | Green light (ns) | Red light (ns) |
|-------------------------|------------------|----------------|
| GN/GQD-S | 5.78 | --- |
| GN/RQD-S | --- | 8.95 |
| GN/GQD-P (//, \perp) | 4.96, 4.88 | --- |
| GN/RQD-P (//, \perp) | --- | 8.46, 8.34 |
| QW/GQD-S | 6.48 | --- |
| QW/RQD-S | --- | 9.58 |
| QW/GQD-P (//, \perp) | 6.11, 6.01 | --- |
| QW/RQD-P (//, \perp) | --- | 9.16, 9.13 |

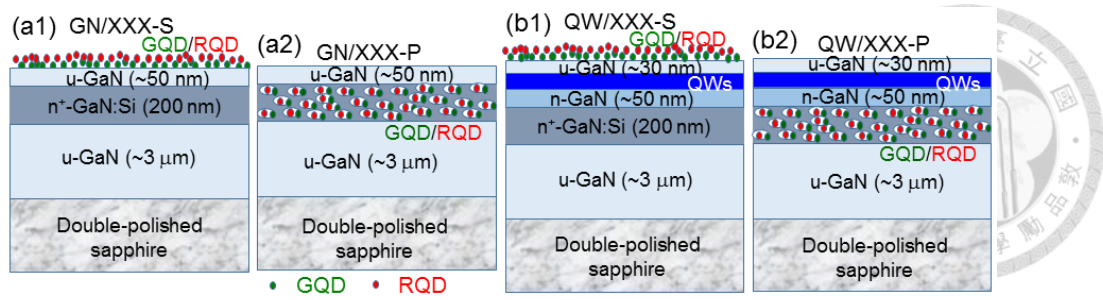


Fig 1.1 Structures of the four sample groups.

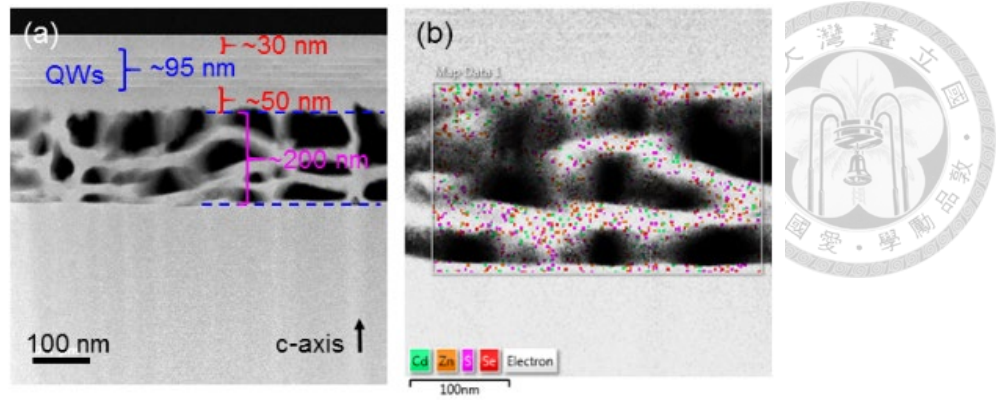
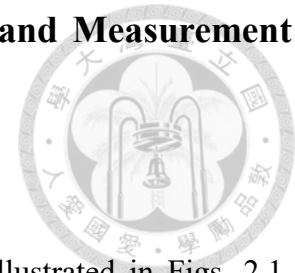


Fig 1.2 TEM and EDX images of a PS with inserted QDs.

Chapter 2 Sample Structures, Fabrication Procedures, and Measurement Methods



2.1 Epitaxial structure

The epitaxial structure for sample fabrication is schematically illustrated in Figs. 2.1, which is designated as epitaxial structure Po-XX. In the structure, with metalorganic chemical vapor deposition (MOCVD), a $\sim 1\text{-}\mu\text{m}$ u-GaN is first deposited on a double-polished sapphire substrate, followed by a $\sim 1.5\text{-}\mu\text{m}$ n-GaN layer growth for serving as the current conduction layer, and a $\sim 100\text{-nm}$ u-GaN layer deposition for separating the PS and current conduction layers. Above the $\sim 100\text{-nm}$ u-GaN layer, a high-conductivity n^{++} -GaN layer and a u-GaN capping layer are grown in either epitaxial structure. The thicknesses of the n^{++} -GaN and u-GaN layers are 600 and 300 nm, respectively. The total thickness of the layers above the n-GaN layer is 1000 nm. The growth temperatures for all the layers, including u-GaN, n-GaN, and n^{++} -GaN, are the same at 1032 °C. The Si doping concentrations for the layers of n-GaN and n^{++} -GaN are $\sim 5 \times 10^{18}$ and $\sim 5 \times 10^{19} \text{ cm}^{-3}$, respectively.

2.2 Fabrications of mesa and porous structures

The PS is formed in a mesa structure. To make all the etched trenches oriented in a fixed direction, the mesa is designed as a stripe geometry, as schematically illustrated in Fig. 2.2. The width and length of a stripe mesa are 300 micron and 0.9 cm, respectively. Such a mesa is periodically arranged along the direction of its width. The distance between two neighboring mesas is only 5 micron. With such a mesa layout, ECE can form PS trenches from either sidewall of a mesa toward its center along the mesa width direction. In this situation, all the etched PS trenches are parallel and essentially perpendicular to a mesa sidewall except the regions near the two mesa ends. In other words, the etched trenches are oriented in the same direction overall the large central portion of a sample. This portion will be used for optical

measurements.

Figure 2.3 illustrates the setup for ECE. As illustrated, in a container the semiconductor sample connected by copper foil tape with a DC power supply serves as the anode and a platinum wire serves as the cathode in the electrochemical interaction. Only part of the sample is immersed in the electrolyte (5 % HNO₃). The applied voltage of the DC power supply can be adjusted. The electrode of the semiconductor sample contacts the n-GaN layer for current supply. The ECE interaction process is schematically depicted in Fig. 2.4 for a mesa sample. After the electric current flows into the mesa region, to find a current path of the minimized resistance, it flows upward into the n⁺⁺-GaN layer of the mesa through the u-GaN layer because the conductivity of the n⁺⁺-GaN layer is higher than that of the electrolyte. It is noted that although the conductivity of the u-GaN layer is not high, it is indeed conductive. After electric current enters the n⁺⁺-GaN layer, it flows toward the boundary of the mesa and enters the electrolyte to complete the current loop. At the boundary of the mesa, the interaction between electric current and electrolyte starts the ECE process. Once pores are formed in the n⁺⁺-GaN layer, electrolyte flows into the pores for continuing the ECE process. As the process proceeds, the etched trenches of pores extend toward the mesa center.

Figures 2.5(a)-2.5(e) show the fabrication procedures of a sample. As illustrated in Fig. 2.5(a), first photolithography is applied for defining the mesa structure. Then, as illustrated in Fig. 2.5(b), we use inductively coupled plasma reactive ion etching (ICPRIE) to form the mesa structure. The ICPRIE etching depth is ~800 nm. Next, as illustrated in Fig. 2.5(c), an ECE process is applied to form the PS in the originally n⁺⁺-GaN layer. A PS can also be formed in the originally n-GaN layer because electrolyte can enter this layer through threading dislocations. At this stage, the residual photoresist can help in protecting the capping GaN layer during ECE. After that, another ICPRIE process (etching depth ~600 nm) is applied to expose the upper PS by removing the GaN capping layer and part of the PS layer, as illustrated in Fig.

2.5(d). In this situation, the etched oriented trenches can be seen through SEM on the top surface of a sample. Finally, as illustrated in Fig. 2.5(e), the solutions of QDs and Ag NPs are drop-casted onto the sample surface. The QDs and Ag NPs of small sizes can be naturally settled into the trenches.

We purchase green- and red-emitting CdZnSeS/ZnS QDs (designated as GQD and RQD, respectively) for this research from Taiwan Nanocrystals Inc., Hsinchu, Taiwan. Those QDs are capped with poly(isobutylene-alt-maleic anhydride) and hence are negatively charged with zeta potentials in the range from -40 to -50 mV [47]. The emission peak wavelengths of GQD and RQD are 530 and 625 nm, respectively. Including the capping amphiphilic polymer, either GQD or RQD is a sphere-like particle of 8-10 nm in size. The concentration of either a GQD or an RQD solution is 1 mg/mL. Two Ag NP samples of different sizes are chemically synthesized. The smaller Ag NP, which is referred to as GNP, is synthesized by first mixing sodium citrate of 0.075 M in concentration and 2.997 mL in volume, AgNO₃ of 0.1 M in concentration and 0.05 mL in volume, H₂O₂ of 35 % in concentration and 0.12 mL in volume, and de-ionized water of 46.95 mL in volume through stirring at a speed of 360 rpm. Then, NaBH₄ of 0.1 M in concentration and 0.2 mL in volume is added to the solution. Next, another stirring process of 5 min is undertaken for reducing Ag NPs. After removing the residual chemicals in the solution, 2-mL Ag NP solution is mixed with 5 K PEG of 1 mM in concentration and 2 mL in volume for linking each other. The mixed solution is placed in a refrigerator of 4 °C in temperature for 24 hours for completing the linkage. After removing the residual chemicals, GNP sample is ready for use. GNP before linking with PEG is also used as the seed for synthesizing the Ag NP of a larger size, which is referred to as RNP. To fabricate RNP, first we mix de-ionized water of 11 mL in volume, ascorbic acid of 0.1 M in concentration and 0.075 mL in volume, sodium citrate of 0.075 M in concentration and 0.05 mL in volume, and AgNO₃ of 0.1 M in concentration and 0.06 mL in volume with 10-mL GNP solution. After

stirring for 20 min and removing the residual chemicals, we obtain the RNP solution. Again, to protect the Ag NPs, 2-mL RNP solution is mixed with 5 K PEG of 1 mM in concentration and 2 mL in volume for linking each other. The mixed solution is placed in a refrigerator of 4 °C in temperature for 24 hours for completing the linkage. After removing the residual chemicals, RNP sample is ready for use. Due to the complicated synthesis process and non-uniform NP sizes, it is difficult to estimate the NP concentration of the GNP and RNP solutions. The geometry of GNP is close to a sphere with the diameter in the range from 20 to 30 nm. An RNP looks like a nano-disk with the diameter in the range from 50 to 60 nm and the thickness in the range of 10-15 nm.

2.3 Sample designations and structures

Figures 2.6(a)-2.6(c) show the photographs under a microscope of a sample after mesa fabrication, after ECE, and after the second ICPRIE process for exposing the PS, respectively. The parallel lines correspond the separating trenches between stripe mesas. The ECE process is undertaken with 13 V in applied voltage, 5-% HNO₃ as electrolyte, 45 min in reaction duration. During the ECE process, electric current decreases from 4.43 to 0.026 mA. Figures 2.6(d) and 2.6(e) show the photographs of the whole sample after mesa fabrication and after ECE, respectively. The darker region in the sample shown in Fig. 2.6(e) corresponds to the portion of the sample immersed in the electrolyte. PS is formed only in this portion. Figure 2.7(a) also shows a photograph of the sample after the second ICPRIE process for exposing the PS. Figures 2.7(b) and 2.7(c) show the SEM images in the regions roughly circled by the red and blue rectangles in Fig. 2.7(a). In Fig. 2.7(b), one can see a mesa sidewall above which etched PS trenches are essentially parallel and perpendicular to the sidewall. In Fig. 2.7(c), one can see the middle narrow band dividing the two etching regions. The etched PS trenches are perpendicular to this dividing band. Figure 2.7(d) shows the magnified SEM image in the

region circled by the green rectangle in Fig. 2.7(c). Here, one can see that the trench width ranges from 30 through 70 nm.

On the exposed trenched PS shown in Fig. 2.7, we drop-cast the combinations of the water solutions of GQD, RQD, GNP, and RNP to fabricate sample series P-. For comparison, the same solution combinations are drop-casted onto u-GaN templates for forming sample series S-. The solution combinations include GNP, RNP, GQD, RQD, GQD+GNP, RQD+RNP, GQD+RQD, GQD+RQD+GNP, and GQD+RQD+RNP. When a sample includes both QD and Ag NP, the QD solution is drop-casted first, followed by the Ag NP solution. This drop-cast procedure can minimize the lateral spreading of Ag NP on a PS surface. After drop-casting the first solution, the sample is wrapped by aluminum foil and placed in dry environment for naturally drying up the solution that takes about 12 hours. After that, the second solution is drop-casted. GQD and RQD and can be mixed into a single solution for drop-casting when a sample includes both GQD and RQD.

Figures 2.8(a)-2.8(d) show the SEM images of samples S-GQD, S-RQD, S-GNP, and S-RNP, respectively. The size of RQD is about the same as that of GQD. However, the size of RNP is significantly larger than that of GNP. Figure 2.9 shows the normalized photoluminescence (PL) spectra of GQD and RQD, and the normalized extinction spectra of GNP and RNP in water. The PL spectra peaks of GQD and RQD are 530 and 625 nm, respectively. The extinction spectral peaks of GNP and RNP are 512 and 551 nm, respectively. The localized surface plasmon (LSP) resonance peak wavelength of GNP (RNP) in water is shorter than the PL spectral peak wavelength of GQD (RQD). However, after they are applied to a PS, the LSP resonance peaks will be red-shifted due to the higher refractive indices of GaN and QD such that the LSP resonance peak can become closer to the QD emission wavelength. Figures 2.10(a) and 2.10(b) show the SEM images of samples S-GQD+GNP and S-RQD+RNP, respectively. In each figure, the larger (smaller) particles correspond to Ag NP (QD). Figures

2.11(a)-2.11(c) show the SEM images of samples S-GQD+RQD, S-GQD+RQD+GNP, and S-GQD+RQD+RNP, respectively.

Figures 2.12(a)-2.12(d) show the SEM images of samples P-GQD, P-RQD, P-GNP, and P-RNP, respectively. Here, the observed particles correspond to Ag NPs. It is more difficult to see QDs because they are smaller than 10 nm. Also, most of QDs are settled into the trenches of the PS samples. Figures 2.13(a) and 2.13(b) show the SEM images of samples P-GQD+GNP and P-RQD+RNP, respectively. Figures 2.14(a)-2.14(c) show the SEM images of samples P-GQD+RQD, P-GQD+RQD+GNP, and P-GQD+RQD+RNP, respectively. Figure 2.15 shows a dark-field transmission electron microscopy (TEM) image of sample P-GQD+RQD+RNP. Here, we can see that QDs distribute around the sample top. Also, two RNPs can be clearly seen. Figure 2.16(a) shows the energy-dispersive X-ray spectroscopy (EDX) mapping image of the TEM image shown in Fig. 2.15. Figures 2.16(a)-2.16(f) shows the EDX mapping images of Cd, Se, Ag, Zn, and S elements, respectively. The results in Figs. 2.15 and 2.16 confirm the insertions of RNP and QDs into the trench structure of this sample. It is noted that the GaN trench structure near the surface can be somewhat damaged during the focused ion-beam process for preparing the TEM specimen.

2.4 Optical measurements

Figure 2.17 shows the setup for continuous PL measurement. This setup can actually be used for temperature dependent PL measurement. However, in this study, the function of temperature dependent PL measurement is not used. In other words, the cold chamber for accommodating a sample is not used. Here, through an objective, the 405-nm excitation InGaN laser diode is vertically incident upon the sample. The excited PL is collected by the same objective and directed into a fiber bundle through a dichroic mirror. Before PL enters the fiber bundle, the light of the designated polarization is chosen through a polarizer. The polarization

of the excitation laser with respect to the anisotropic sample structure is controlled by rotating the sample orientation. The 405-nm laser diode delivers 6 mW in power for the temperature-dependent PL measurement.

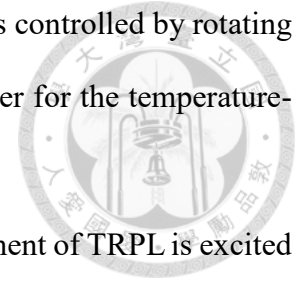


Figure 2.18 shows the setup for TRPL measurement. The measurement of TRPL is excited by the second-harmonic (wavelength at 390 nm and power at 1.5 mW) of a femtosecond Titanium:sapphire laser at 76 MHz in pulse repetition rate. The signals are collected and analyzed by a photon-counting system. The temporal resolution is better than 0.1 ns. The procedure for evaluating the PL decay time was reported in a previous publication [29]. A polarizer is placed before the collected PL enters the photon counter for controlling the PL polarization. Again, the excitation polarization is controlled by rotating the sample under study. TRPL is performed only at room temperature.

Sample Po-XX

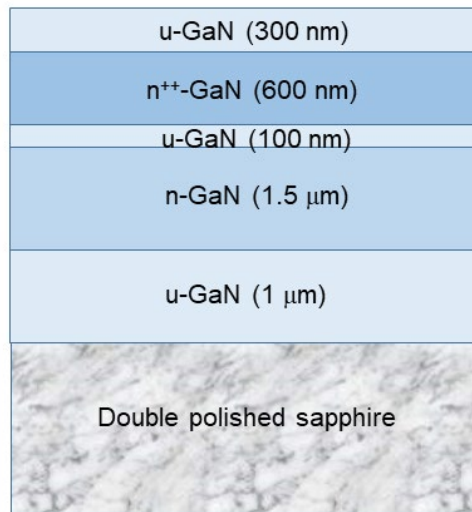


Fig 2.1 Schematic illustration for the epitaxial structure used for sample fabrication, which is designated as epitaxial structure Po-XX.

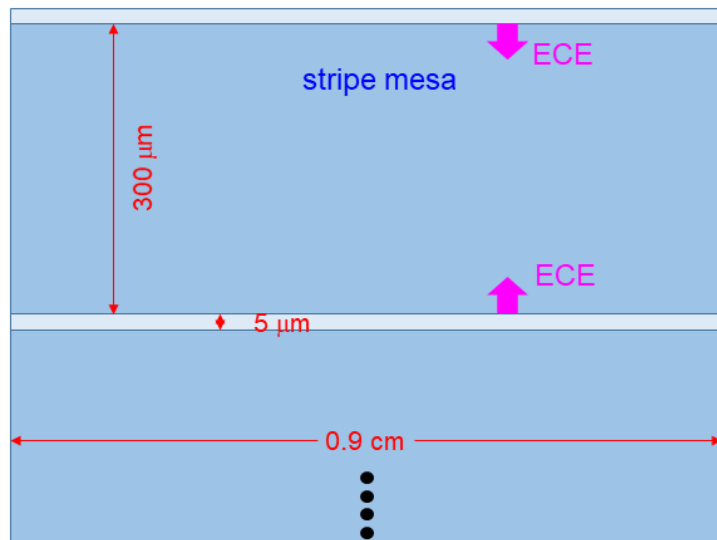


Fig 2.2 Layout of the periodic pattern of stripe mesa.

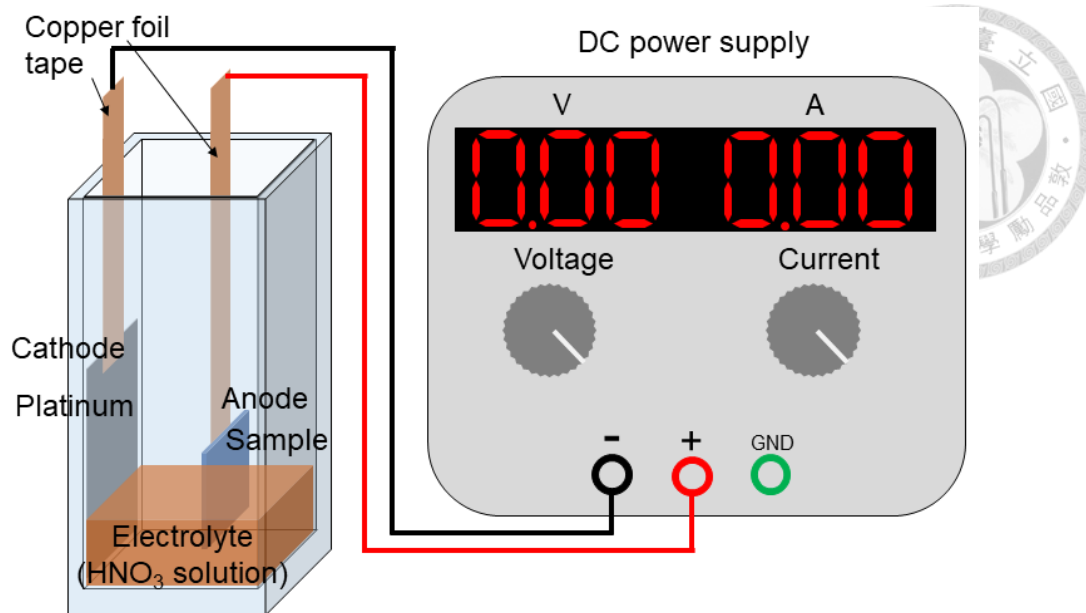


Fig 2.3 Setup for an ECE process.

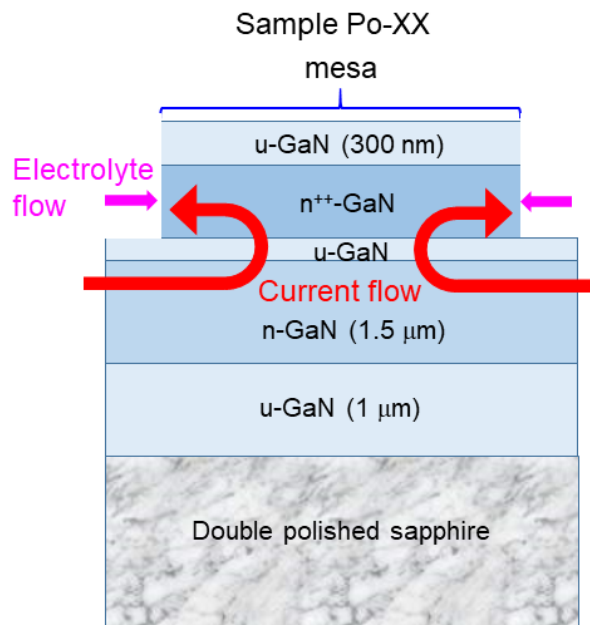


Fig 2.4 Flow paths of applied electric current and electrolyte in an ECE process for etching the conduction layers in a mesa.

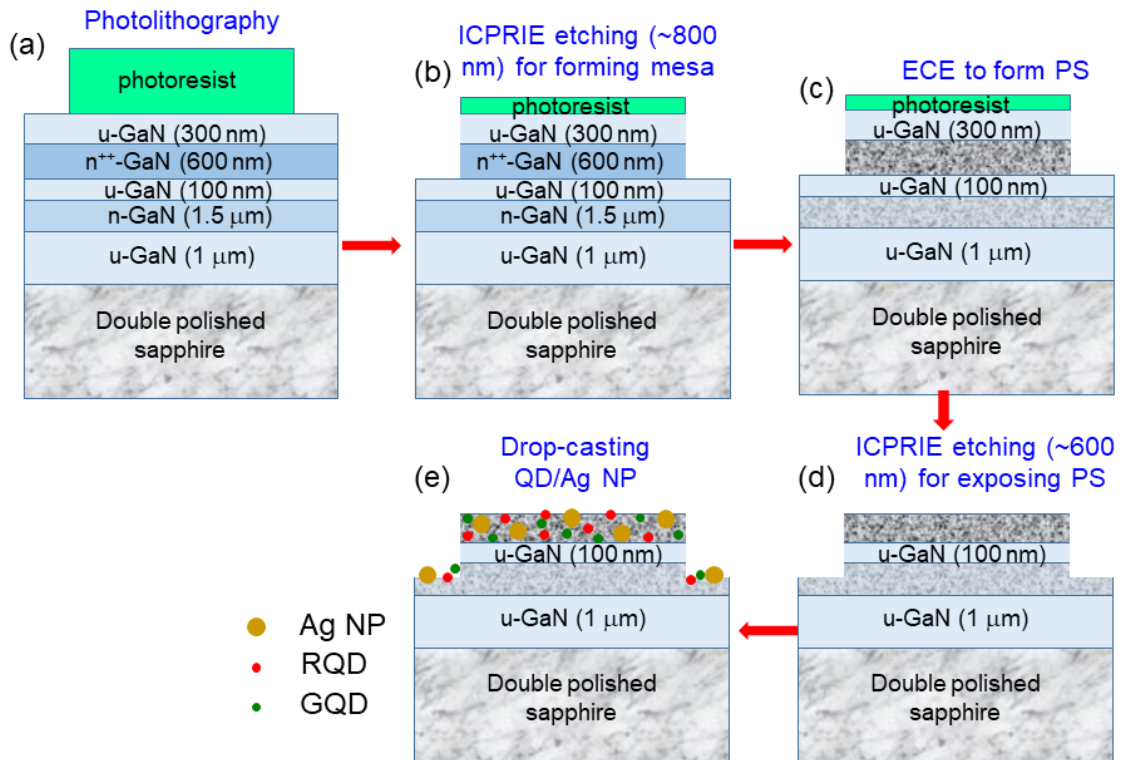
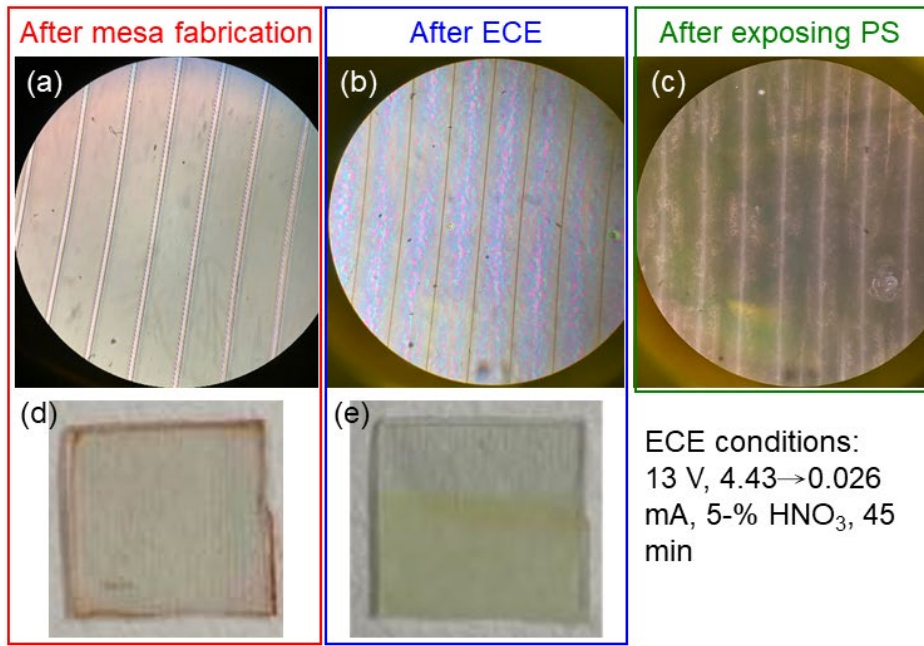


Fig 2.5 (a)-(e): Fabrication procedures of a sample, including photolithography to define mesa (a), ICPRIE to fabricate mesa (b), ECE to form PS (c), another ICPRIE process to expose the upper PS (d), and drop-casting the solutions of QDs and Ag NPs (e).



ECE with Positive PR
Covering Mesa region
(remove PR after ECE)

ICP Etching Exposing
Polarized Porous
Structure

Fig 2.6 (a)-(c): Photographs under a microscope of a sample after mesa fabrication, after ECE, and after the second ICPRIE process for exposing the PS, respectively. (d) and (e): Photographs of the whole sample after mesa fabrication and after ECE, respectively.

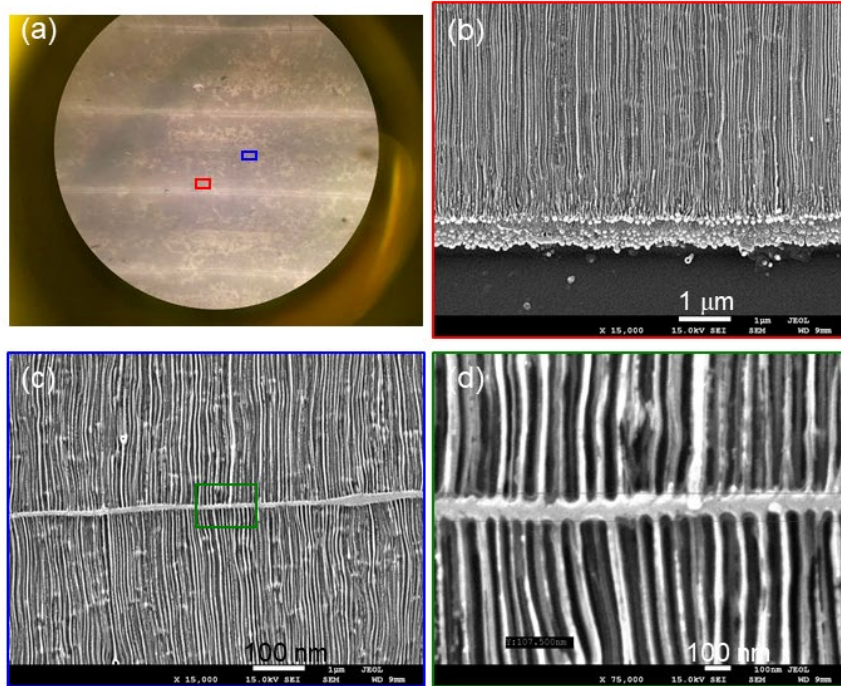


Fig 2.7 (a): Photograph of a sample after the second ICPRIE process for exposing the PS. (b) and (c): SEM images in the regions roughly circled by the red and blue rectangles in part (a). (d): Magnified SEM image in the region circled by the green rectangle in part (c).

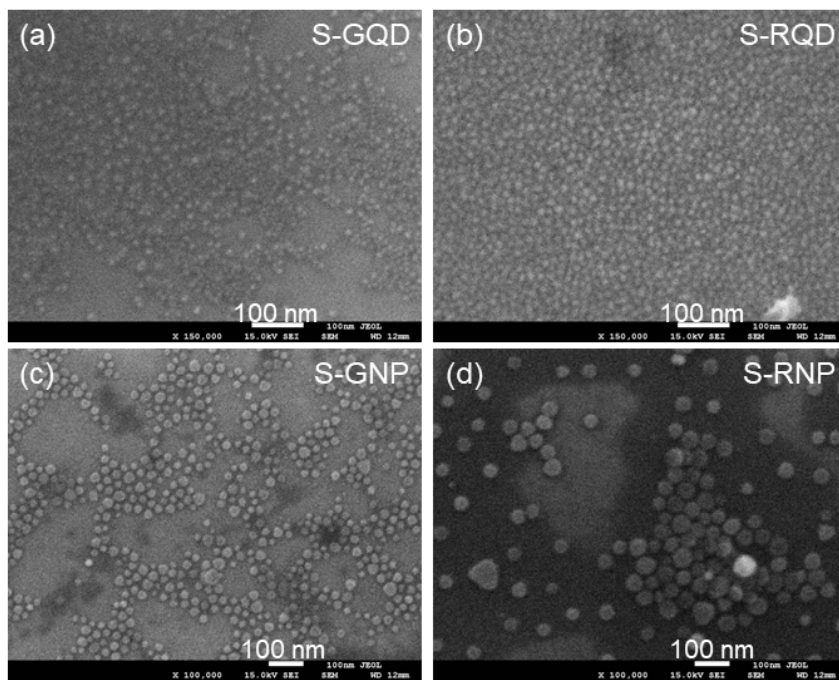


Fig 2.8 (a)-(d): SEM images of samples S-GQD, S-RQD, S-GNP, and S-RNP, respectively.

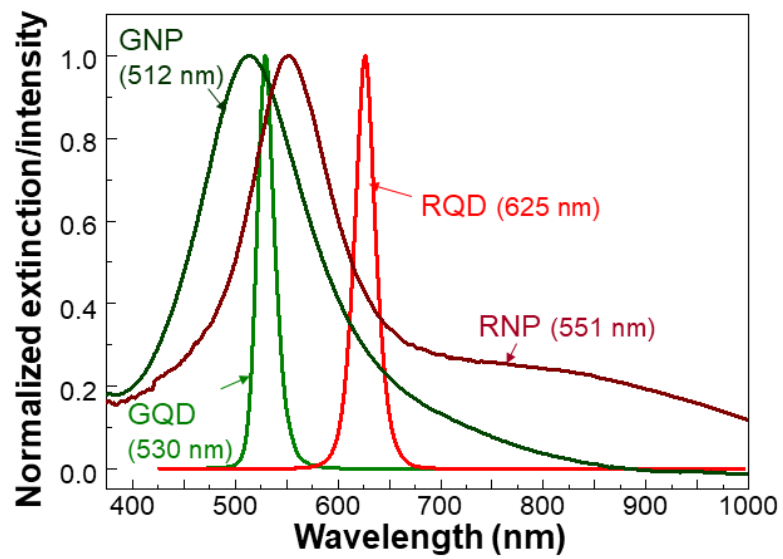


Fig 2.9 Normalized PL spectra of GQD and RQD, and the normalized extinction spectra of GNP and RNP in water.

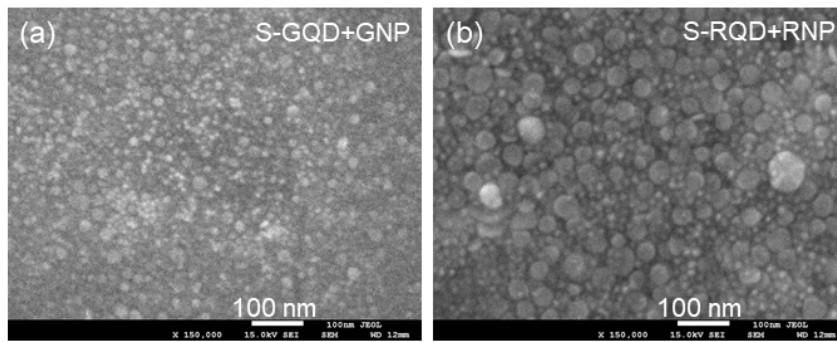


Fig 2.10 (a) and (b): SEM images of samples S-GQD+GNP and S-RQD+RNP, respectively.

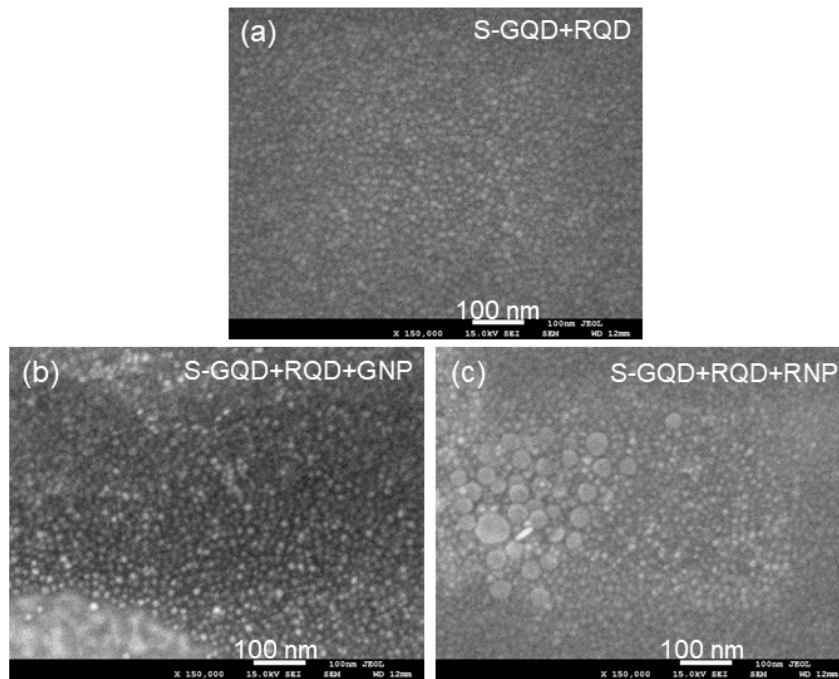


Fig 2.11 (a)-(c): SEM images of samples S-GQD+RQD, S-GQD+RQD+GNP, and S-GQD+RQD+RNP, respectively.

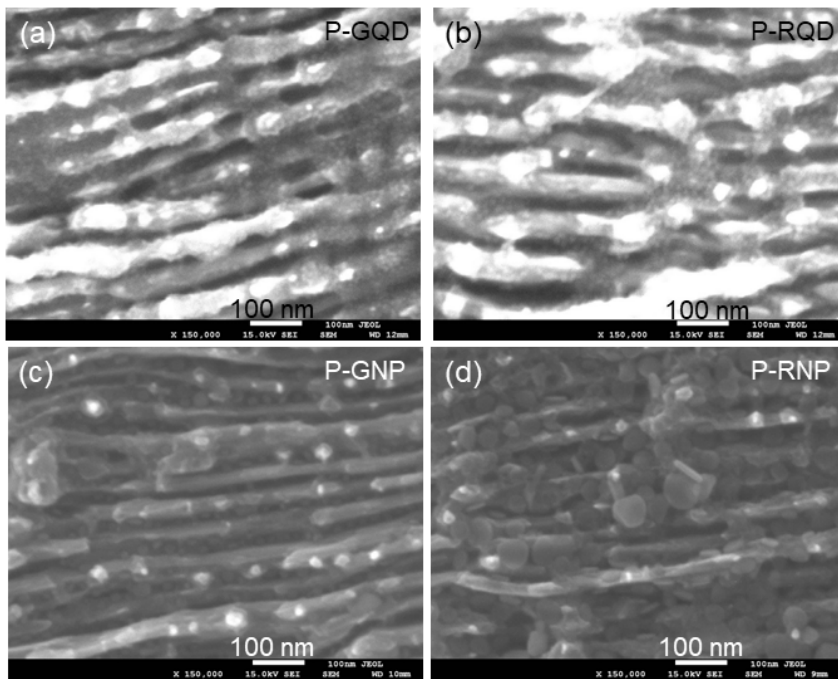


Fig 2.12 (a)-(d): SEM images of samples P-GQD, P-RQD, P-GNP, and P-RNP, respectively.

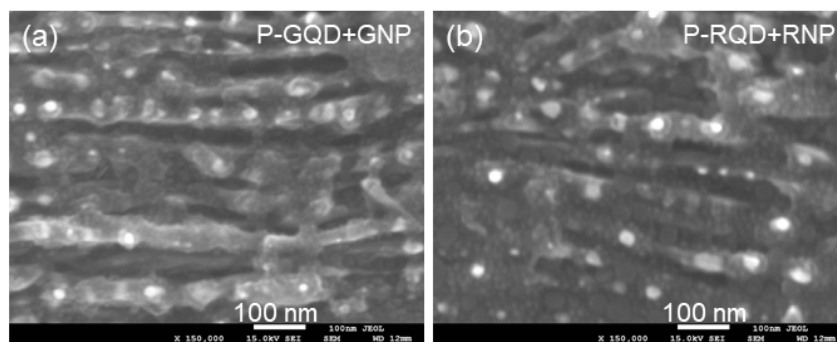


Fig 2.13 (a) and (b): SEM images of samples P-GQD+GNP and P-RQD+RNP, respectively.

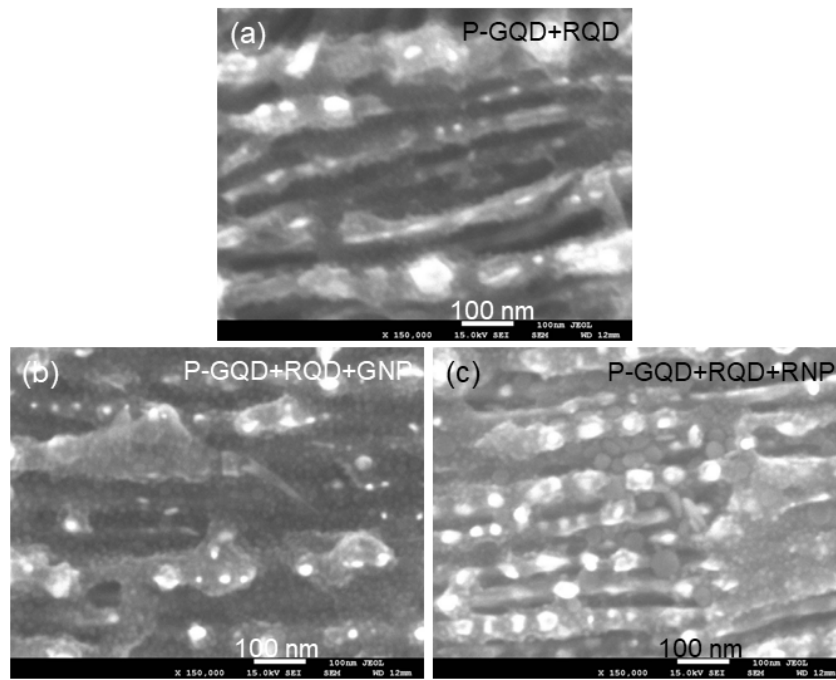


Fig 2.14 (a)-(c): SEM images of samples P-GQD+RQD, P-GQD+RQD+GNP, and P-GQD+RQD+RNP, respectively.

Sample P-GQD+RQD+RNP

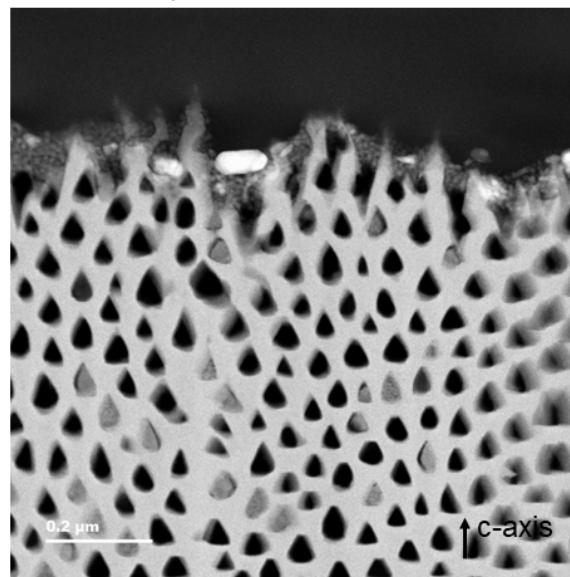


Fig 2.15 Cross-sectional TEM image of sample P-GQD+RQD+RNP.

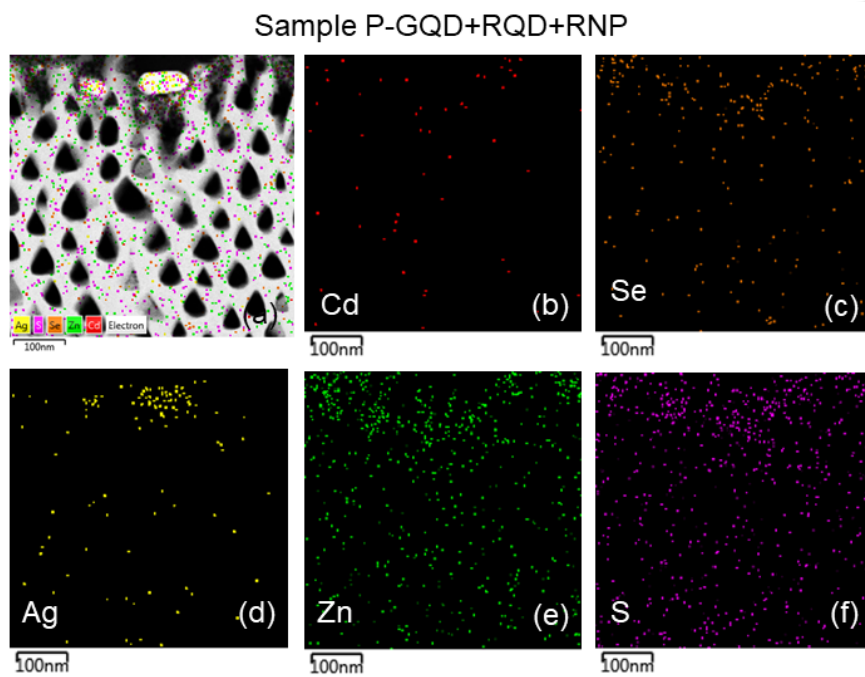


Fig 2.116 (a): EDX mapping of a TEM image of sample P-GQD+RQD+RNP. (b)-(f): EDX mappings of elements Cd, Se, Ag, Zn, and S.

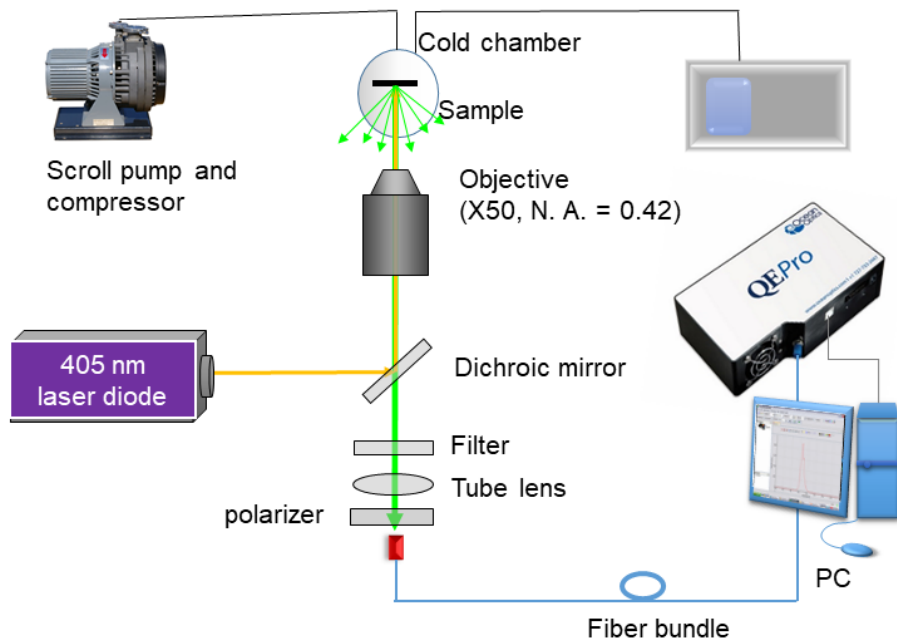


Fig 2.17 Setup for continuous PL measurement.

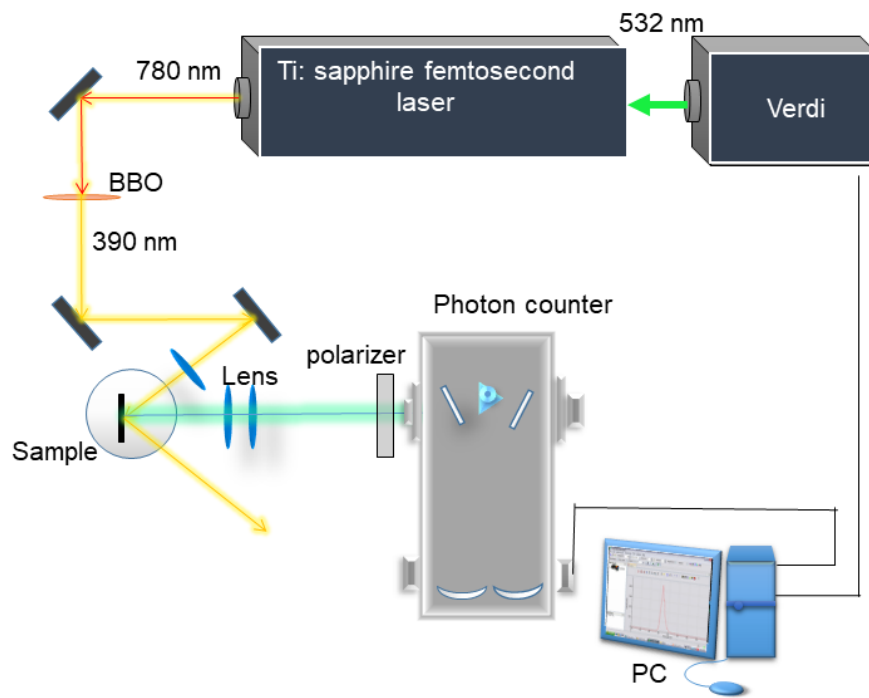


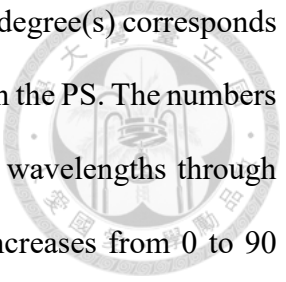
Fig 2.18 Setup for time-resolved PL measurement.

Chapter 3 Polarization Dependent Optical Measurement Results

3.1 Polarization dependent localized surface plasmon resonance

The localized surface plasmon (LSP) resonance behaviors of the Ag NPs in the samples are studied with polarization dependent transmission measurement. A depression in a transmission spectrum corresponds to the LSP resonance feature. Figures 3.1(a)-3.1(c) show the transmission spectra of samples S-GNP, S-GQD+GNP, and S-GQD+RQD+GNP, respectively, which are obtained by using a GaN template, samples S-GQD and S-GQD+RQD as the normalization bases, respectively. Here, the vertical green and red dashed lines show the emission wavelengths of GQD and RQD, respectively. As shown in Fig. 2.9, the extinction peak of GNP in water is 512 nm. After drop-casting GNP on the surface of a GaN template, the LSP resonance peak is red-shifted to 567 nm, as shown in Fig. 3.1(a) due to the higher refractive index of GaN (~ 2.4). After adding GQD to the GaN surface, the LSP resonance peak is further red-shifted to 569 nm. Then, by further adding RQD to the surface sample, it is further red-shifted to 580 nm. Figures 3.2(a)-3.2(c) show the transmission spectra of samples S-RNP, S-RQD+RNP, and S-GQD+RQD+RNP, respectively, which are obtained by using a GaN template, samples S-RQD and S-GQD+RQD as the normalization bases, respectively. As shown in Fig. 2.9, the extinction peak of RNP in water is 551 nm. After drop-casting RNP on the surface of a GaN template, the LSP resonance peak is red-shifted to 605 nm, as shown in Fig. 3.2(a) due to the higher refractive index of GaN (~ 2.4). After adding RQD to the GaN surface, the LSP resonance peak is further red-shifted to 632 nm. Then, by further adding RQD to the surface sample, it is maintained at around 632 nm. Generally speaking, by placing GNP and/or RNP with GQD and/or RQD on GaN, their LSP resonance spectral ranges well cover the emission wavelengths of GQD and RQD, respectively.

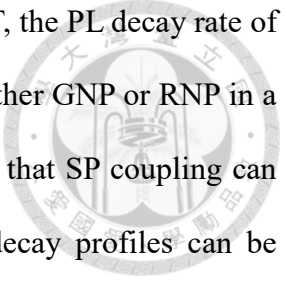
Figure 3.3 shows the transmission spectra of sample P-GNP under different polarization conditions, including the polarization directions tilted 0, 30, 60 and 90 degrees with respect to



the PS trench orientation. In other words, the polarization angle of 0 (90) degree(s) corresponds to the polarization parallel with (perpendicular to) the trench orientation in the PS. The numbers after polarization angles in the labels show the transmission minimum wavelengths through Gaussian fitting. Here, one can see that when the polarization angle increases from 0 to 90 degrees, the transmission minimum wavelength blue shifts from 542 to 531 nm although the variation is not necessarily monotonic. Also, as the polarization angle increases, the transmission depression becomes deeper, indicating that the LSP resonance becomes stronger. In other words, the LSP resonance is the strongest when the polarization is perpendicular to the trench orientation. It is noted that because of the rough structure of the sample, strong fluctuations exist in the transmission spectra such that it is difficult to calibrate the transmission depression minima. As indicated by the dashed curves in Fig. 3.3, we use a Gaussian line to fit each data curve to roughly indicate the transmission minimum. In Fig. 3.3, we also show the un-polarized transmission spectrum. Again, the vertical green and red dashed lines show the emission wavelengths of GQD and RQD, respectively. Figures 3.4-3.8 show the results similar to those in Fig. 3.3 for samples P-GQD+GNP, P-GQD+RQD+GNP, P-RNP, P-RQD+RNP, and P-GQD+RQD+RNP, respectively. All the samples show the same polarization-dependent variation trend. As the polarization angle increases from 0 to 90 degrees, the LSP resonance feature always blue shifts. Generally, the LSP resonance wavelengths of RNP are longer than those of GNP. The causes for the polarization dependence behaviors of GNP and RNP will be discussed latter.

3.2 Polarization dependent time-resolved photoluminescence of quantum dots

Time-resolved photoluminescence (PL) measurement can provide us with the information of QD emission efficiency. Figures 3.9(a) and 3.9(b) show the normalized PL decay profiles of the green and red components, respectively, for all those plane surface samples. Here, one can

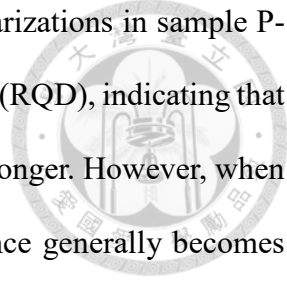


see that with GQD and RQD coexistent in a sample for producing FRET, the PL decay rate of the green (red) component becomes higher (lower). Meanwhile, with either GNP or RNP in a sample, the decay rate of either green or red light increases, indicating that SP coupling can indeed enhance QD emission efficiency. The decay times of those decay profiles can be calibrated based on an extended-exponential model [29]. Table 3.1 shows the PL decay times of the green and red components of all the samples fabricated on a flat GaN surface. By combining GNP (RNP) with GQD (RQD) on the surface, the green (red) PL decay time reduces from 7.111 (10.518) to 6.271 (8.927) ns through SP coupling. The PL decay rate enhancement percentage of green (red) light is 13.4 (17.8) %, as shown inside the parentheses in Table 3.1. Those increments can be regarded as the enhancements of QD emission efficiency since the non-radiative recombination rate of QD is unchanged. In sample S-GQD+RQD, through FRET, the decay time of green (red) light is reduced (increased) to 4.313 (13.915) ns. The FRET efficiency is evaluated to give 39.35 %, as shown inside the curly brackets. The FRET efficiency, η , is defined as $\eta = 1 - \tau_{DA}/\tau_D$ [48]. Here, τ_{DA} is the PL decay time of the energy donor when the acceptor exists and τ_D is that when the acceptor is absent. For the FRET process in sample S-GQD+RQD, τ_{DA} (τ_D) is the PL decay time of sample S-GQD+RQD (S-GQD). As shown in row 7 of Table 3.1, in sample S-GQD-RQD-GNP, the PL decay time of either green or red light is reduced due to the SP coupling of GNP. In this situation, the FRET efficiency is reduced, when compared with that of sample S-GQD+RQD. It is noted that SP coupling can either strengthen or weaken an involved FRET process. As shown in row 8 of Table 3.1, in sample S-GQD-RQD-RNP, the PL decay time of either green or red light is longer than the corresponding value in sample S-GQD+RQD+GNP, indicating that here the SP coupling of RNP is relatively weaker than that of GNP.

Figures 3.10(a) and 3.10(b) show the normalized PL decay profiles of the green and red lights, respectively, for the samples with PSs under the conditions of polarized excitation, but

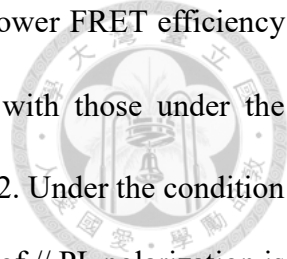
un-polarized PL. The \perp and \parallel signs in the labels represent the excitation polarizations perpendicular to and parallel with the trench orientation. In Fig. 3.10(a), we can see that the green-light decay becomes faster after GNP is added to a sample with GQD. With both GQD and RQD in a sample, the induced FRET leads to a significant increase of PL decay rate. As shown in Fig. 3.10(b) for the red-light component, SP coupling induced by RNP results in a significant increase of PL decay rate. Also, FRET makes the red-light PL decay slowed down. In the same sample, the difference between the two excitation polarization conditions is generally small. However, those in the samples with SP coupling are larger. Figures 3.11(a) and 3.11(b) show the normalized PL decay profiles of the green and red lights, respectively, for part of the PS samples under the conditions of polarized excitation and polarized PL. Again, the \perp and \parallel signs in the figures represent the polarizations perpendicular to and parallel with the trench orientation, respectively, for either excitation or PL. In the labels, the first (second) sign describes the excitation (PL) polarization. Figure 3.11(a) shows the results of samples P-GQD, P-GQD+GNP, and P-GQD+RQD. Figure 3.11(b) shows the results of samples P-RQD, P-RQD+RNP, and P-GQD+RQD. In each figure, the four decay profiles of the same sample with different polarization combinations are close to each other. Figures 3.12(a) and 3.12(b) show the normalized PL decay profiles of the green and red lights, respectively, for the rest of the PS samples under the conditions of polarized excitation and polarized PL, including samples P-GQD+RQD+GNP and P-GQD+RQD+RNP. Again, the four decay profiles of the same sample with different polarization combinations are close to each other. Therefore, we can see two groups of decay profiles in each figure.

Table 3.2 shows the PL decay times of the green and red components of the PS samples under the conditions of polarized excitation, but un-polarized PL. Here, one can see that for either green or red light, the PL decay time under \perp excitation polarization is always shorter than that under \parallel excitation polarization even though their differences are not large. The PL



decay rate difference between the two cases of different excitation polarizations in sample P-GQD+GNP (P-RQD+RNP) is relatively larger than that in sample GQD (RQD), indicating that SP coupling in the polarization perpendicular to trench orientation is stronger. However, when FRET occurs in those samples with both GQD and RQD, the difference generally becomes smaller. Again, in Table 3.2, the numbers inside the parentheses show the enhancement percentages of PL decay rate through the SP coupling of either GNP or RNP. We can see that the SP coupling of RNP with RQD is stronger than that of GNP with GQD. As shown inside the curly brackets in Table 3.2, the FRET efficiencies under the condition of // excitation polarization are generally higher than that under the condition of \perp excitation polarization. Also, the SP coupling of GNP can enhance the efficiency of the FRET from GQD into RQD in the PS.

Table 3.3 shows the PL decay times of the green and red components of the samples with PSs under the conditions of polarized excitation and polarized PL. In each box, the numbers before (after) the slash correspond to the results under the condition of \perp (//) PL polarization. Here, just like the results shown in Table 3.2, the PL decay times under the condition of \perp excitation polarization are always shorter than the corresponding values under the condition of // excitation polarization. The PL decay times of the two PL polarizations in each box are close to each other. No systematic trend can be found in their relative levels. However, we can see clear variation trends in PL decay rate enhancement percentage through SP coupling (see the values inside the parentheses) and FRET efficiency (see the values inside curly brackets). The trend of the higher PL decay rate enhancement percentages through SP coupling under the condition of \perp excitation polarization, when compared with those under the condition of // excitation polarization, is consistent with that in Table 3.2. Furthermore, under either excitation polarization, the PL decay rate enhancement percentages through SP coupling under the condition of // PL polarization is always higher than the corresponding values under the



condition of \perp PL polarization. On the other hand, the trend of the lower FRET efficiency under the condition of \perp excitation polarization, when compared with those under the condition of $//$ excitation polarization, is consistent with that in Table 3.2. Under the condition of \perp excitation polarization, the FRET efficiency under the condition of $//$ PL polarization is higher than that under the condition of \perp PL polarization. However, under the condition of $//$ excitation polarization, the FRET efficiency under the condition of \perp PL polarization is higher than that under the condition of $//$ PL polarization. Although their differences are small, the variation trend is clear. Although such a complicated system requires further investigation, a simple attribution deserves mentioning here. Under the condition of \perp excitation polarization, the donor emission efficiency is increased such that the energy available for energy transfer in FRET is reduced and hence the FRET efficiency is decreased. Such a mechanism becomes stronger when SP coupling is introduced.

3.3 Polarization dependent continuous photoluminescence measurement

Whenever both GQD and RQD exist in a sample, FRET can occur and color conversion from green into red can be observed. We measure the continuous PL spectra of those samples with both GQD and RQD for studying the color conversion behaviors under different SP coupling conditions. The color conversion efficiency can be understood by evaluating the integrated intensity ratio of the red component over the green component. Figure 3.13 shows the normalized PL spectra of the three surface samples with both GQD and RQD. They are normalized with respect to the peak intensities of individual green components. From such a curve, we can evaluate the red-over-green integrated intensity ratio (R/G ratio). Among the three surface samples, sample S-GQD+RQD+RNP has the highest red intensity or R/G ratio, followed by sample S-GQD+RQD+GNP, and then sample S-GQD+RQD. The order of red

intensity indicates that RNP can more significantly enhance color conversion, when compared with GNP.

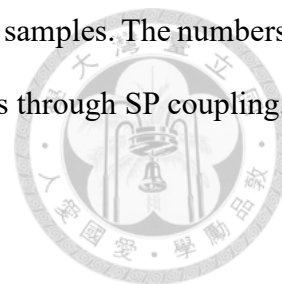
Figures 3.14(a) and 3.14(b) show the normalized PL spectra of the PS samples when the excitation polarization is perpendicular to trench orientation. The results in Fig. 3.14(a) [Fig. 3.14(b)] are obtained under the condition of un-polarized (polarized) PL. In either case, the R/G ratio is highest in sample P-GQD+RQD+RNP, followed by sample P-GQD+RQD+GNP, and then sample P-GQD+RQD. In Fig. 3.14(b), the two spectra of the same sample but different PL polarizations are close to each other. Generally, the order of R/G ratio among the three samples is the same as those shown in Fig. 3.13 and Fig. 3.14(a). Figures 3.15(a) and 3.15(b) show the normalized PL spectra of the PS samples, similar to those in Figs. 3.14(a) and 3.14(b), respectively, when the excitation polarization is parallel with trench orientation. The variation behaviors among different samples and different polarization conditions are similar to those in Figs. 3.14(a) and 3.14(b).

Table 3.4 shows the R/G ratios under various conditions shown in Figs. 3.13-3.15. Again, under all conditions, the orders of R/G ratio among the three samples are the same. Sample with GQD+RQD+RNP is the highest, followed by sample with GQD+RQD+GNP, and then sample with GQD+RQD. The R/G ratios in the PS samples are always higher than the corresponding values in the surface samples. Also, those under the condition of \perp excitation polarization are always higher than the corresponding values under the condition of $//$ excitation polarization. Meanwhile, under either excitation polarization condition, the R/G ratios under the condition of $//$ PL polarization are always higher than the corresponding values under the condition of \perp PL polarization. Such a variation trend does not seem to be consistent with that of FRET efficiency shown in Table 3.3. However, it is reasonable because the color conversion efficiency consists of two factors, including FRET efficiency and acceptor emission efficiency. There is a complicated combination between those two factors, leading to the color

conversion results shown in Table 3.4.

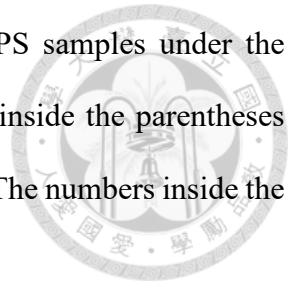


Table 3.1 PL decay times of the green and red components in the surface samples. The numbers inside the parentheses show the PL decay rate enhancement percentages through SP coupling. The numbers inside the curly brackets show the FRET efficiencies.



| sample | Decay time (ns) -- green | Decay time (ns) -- red |
|---------------|--------------------------|------------------------|
| S-GQD | 7.111 | --- |
| S-GQD+GNP | 6.271 (13.4 %) | --- |
| S-RQD | --- | 10.518 |
| S-RQD+RNP | --- | 8.927 (17.8 %) |
| S-GQD+RQD | 4.313 {39.35 %} | 13.915 |
| S-GQD+RQD+GNP | 3.884 {38.06 %} | 11.107 |
| S-GQD+RQD+RNP | 4.145 | 11.538 |

Table 3.2 PL decay times of the green and red components in the PS samples under the conditions of polarized excitation, but un-polarized PL. The numbers inside the parentheses show the PL decay rate enhancement percentages through SP coupling. The numbers inside the curly brackets show the FRET efficiencies.

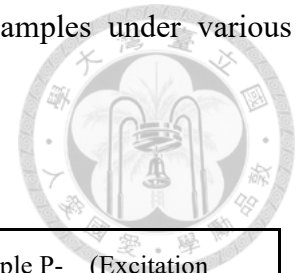


| Excitation polarization | Decay time (ns) -- green | | Decay time (ns) -- red | |
|-------------------------|--------------------------|-----------------|------------------------|----------------|
| | ⊥ to trench | // with trench | ⊥ to trench | // with trench |
| P-GQD | 6.942 | 7.089 | --- | --- |
| P-GQD+GNP | 5.913 (17.3 %) | 6.171 (14.8 %) | --- | --- |
| P-RQD | --- | --- | 8.987 | 9.069 |
| P-RQD+RNP | --- | --- | 6.923 (29.8 %) | 7.370 (23.0 %) |
| P-GQD+RQD | 4.361 {37.17 %} | 4.412 {37.75 %} | 10.543 | 10.711 |
| P-GQD+RQD+GNP | 3.507 {40.68 %} | 3.540 {42.63 %} | 8.233 | 8.397 |
| P-GQD+RQD+RNP | 3.839 | 3.901 | 8.985 | 9.024 |

Table 3.3 PL decay times of the green and red components in the PS samples under the conditions of polarized excitation and polarized PL. The numbers before (after) the slashes show the PL decay times under the condition of \perp ($//$) PL polarization. The numbers inside the parentheses show the PL decay rate enhancement percentages through SP coupling. The numbers inside the curly brackets show the FRET efficiencies.

| Excitation polarization | Decay time (ns) -- green | | Decay time (ns) -- red | |
|-------------------------|-------------------------------------|-------------------------------------|-----------------------------------|-----------------------------------|
| | \perp to trench | $//$ with trench | \perp to trench | $//$ with trench |
| P-GQD | 6.928/7.007 | 7.108/7.051 | --- | --- |
| P-GQD+GNP | 6.107 (13.4 %)/ 6.135 (14.2 %) | 6.404 (11.0 %)/ 6.317 (11.6 %) | --- | --- |
| P-RQD | --- | --- | 9.010/9.051 | 9.219/9.300 |
| P-RQD+RNP | --- | --- | 7.183 (25.4 %)/ 7.121 (27.1 %) | 7.381 (24.9 %)/ 7.434 (25.1 %) |
| P-GQD+RQD | 4.393 {36.59 %}/ 4.410 {37.06 %} | 4.465 {37.19 %}/ 4.437 {37.08 %} | 10.594/10.608 | 10.772/10.793 |
| P-GQD+RQD+GNP | 3.482 {42.99 %}/ 3.482 {43.25 %} | 3.574 {44.19 %}/ 3.579 {43.34 %} | 8.277/8.264 | 8.376/8.287 |
| P-GQD+RQD+RNP | 3.919/3.923 | 3.965/3.927 | 8.775/8.764 | 8.828/8.878 |

Table 3.4 R/G integrated intensity ratios in the surface and PS samples under various polarization combination conditions.



| | Sample S- un-polar. | Sample P- (Excitation polarization \perp to trench) | | | Sample P- (Excitation polarization // with trench) | | |
|-----------------|------------------------|--|---------|------|---|---------|------|
| | | un-polar. | \perp | // | un-polar. | \perp | // |
| PL polarization | --- | un-polar. | \perp | // | un-polar. | \perp | // |
| GQD+RQD | 3.83 | 5.76 | 5.77 | 5.88 | 5.53 | 5.35 | 5.42 |
| GQD+RQD+GNP | 4.70 | 6.03 | 5.89 | 6.09 | 5.79 | 5.82 | 5.93 |
| GQD+RQD+RNP | 5.74 | 6.80 | 6.69 | 6.93 | 6.59 | 6.35 | 6.52 |

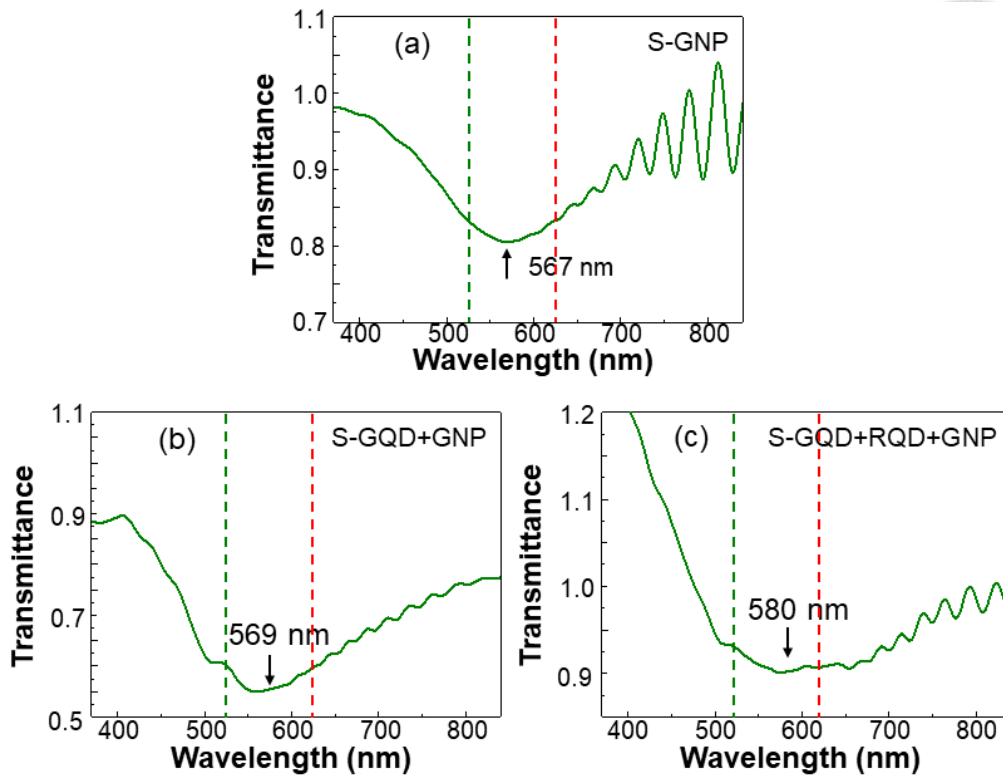


Fig 3.1 (a)-(c): Transmission spectra of samples S-GNP, S-GQD+GNP, and S-GQD+RQD+GNP, respectively, by using a GaN template, samples S-GQD and S-GQD+RQD as the normalization bases, respectively. The vertical green and red dashed lines indicate the emission peak wavelengths of GQD and RQD, respectively.

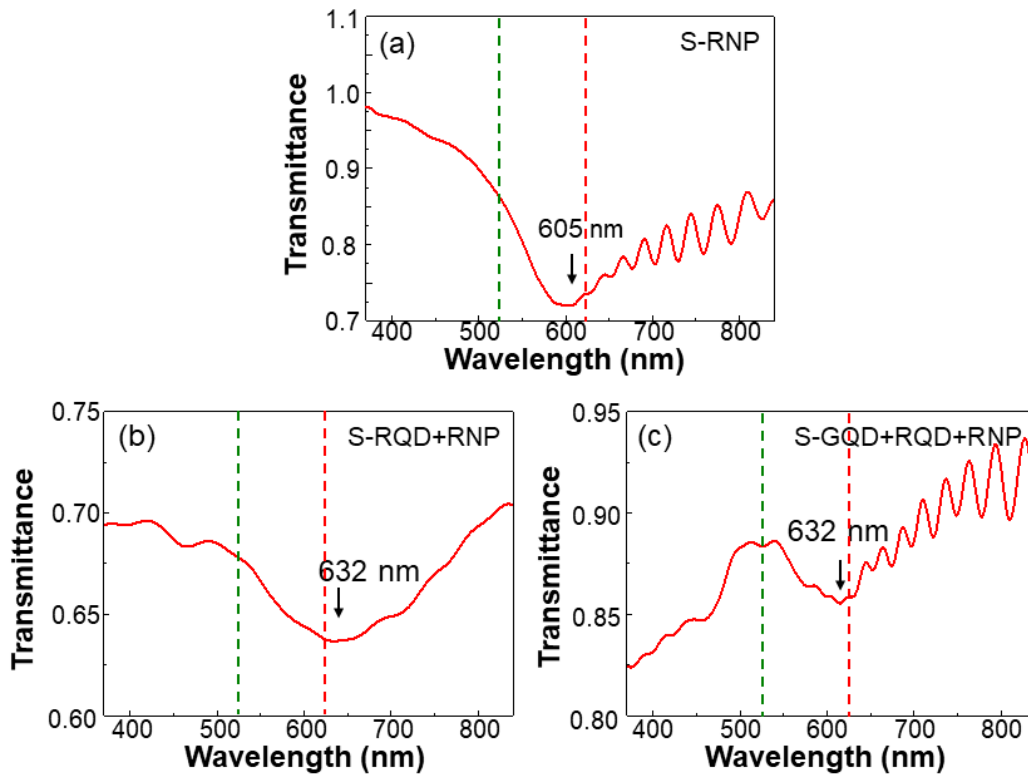


Fig 3.2 (a)-(c): Transmission spectra of samples S-RNP, S-RQD+RNP, and S-GQD+RQD+RNP, respectively, by using a GaN template, samples S-RQD and S-GQD+RQD as the normalization bases, respectively.

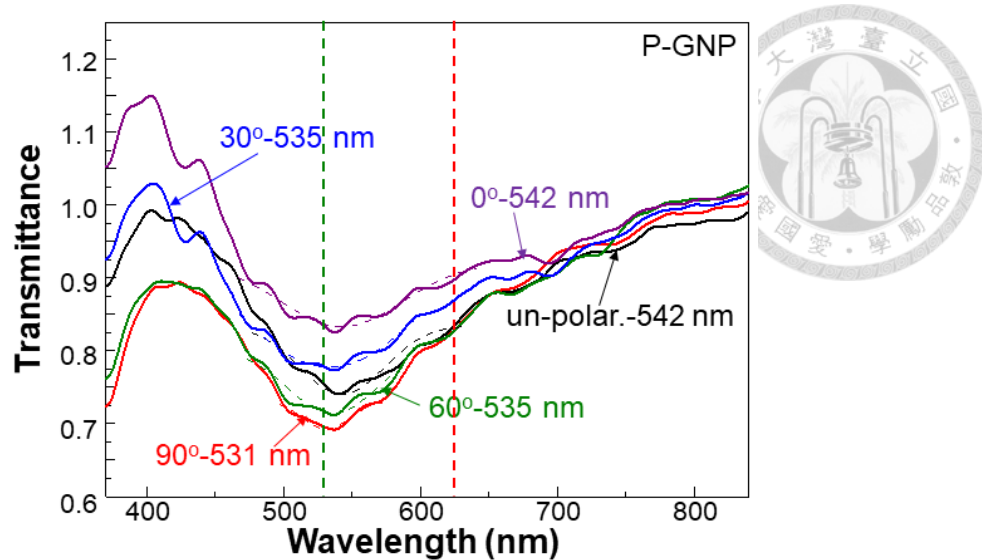


Fig 3.3 Transmission spectra of sample P-GNP under different polarization conditions, including the polarization directions tilted 0, 30, 60 and 90 degrees with respect to the PS trench orientation. The un-polarized transmission spectrum is also shown. The numbers after polarization angles in the labels show the transmission minimum wavelengths through Gaussian fitting.

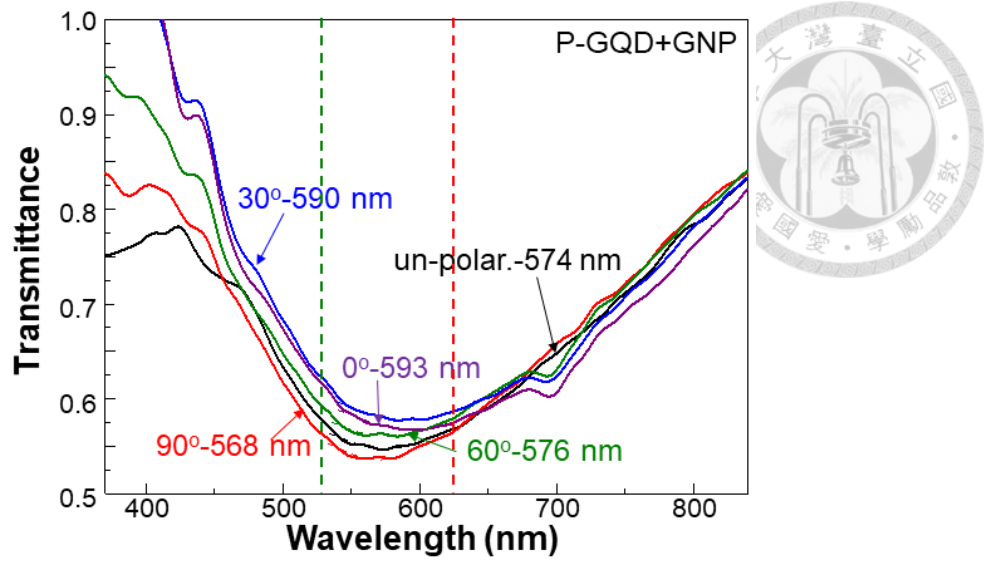


Fig 3.4 Results similar to those in Fig. 3.3 for sample P-GQD+GNP.

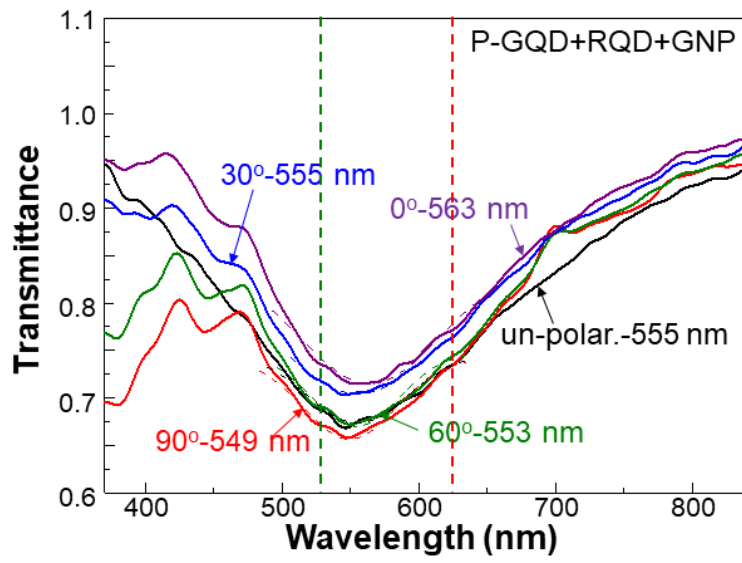


Fig 3.5 Results similar to those in Fig. 3.3 for sample P-GQD+RQD+GNP.

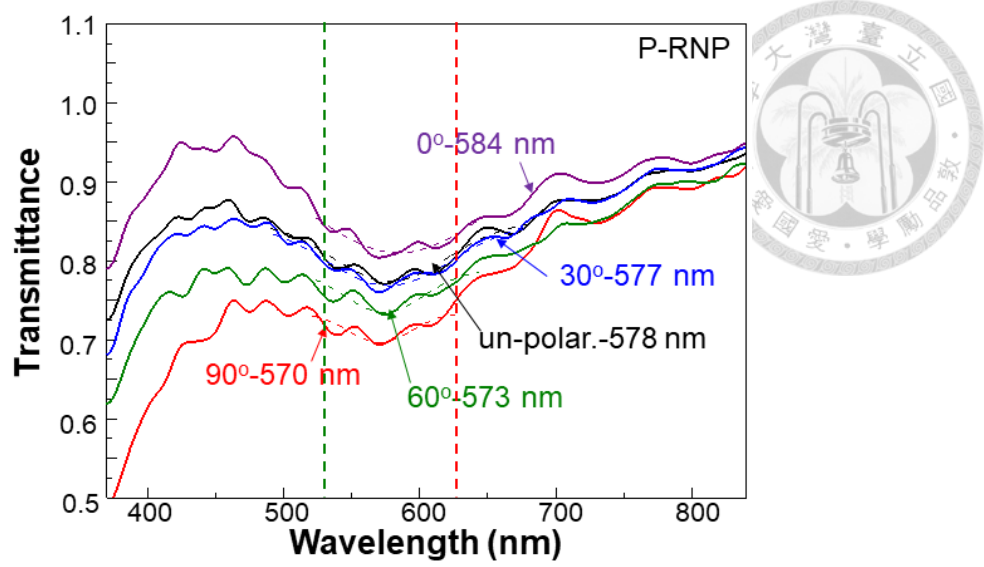


Fig 3.6 Results similar to those in Fig. 3.3 for sample P-RNP.

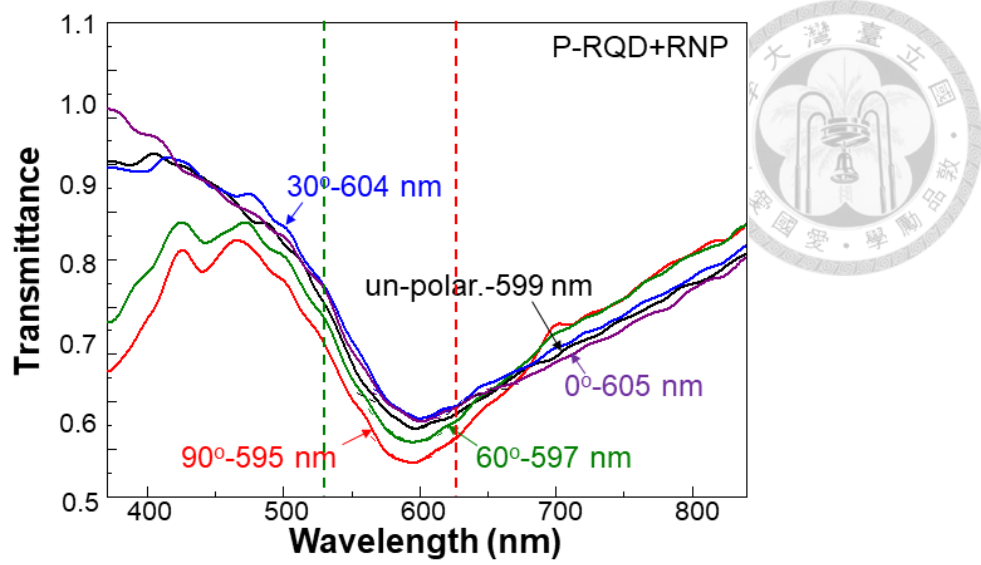


Fig 3.7 Results similar to those in Fig. 3.3 for sample P-RQD+RNP.

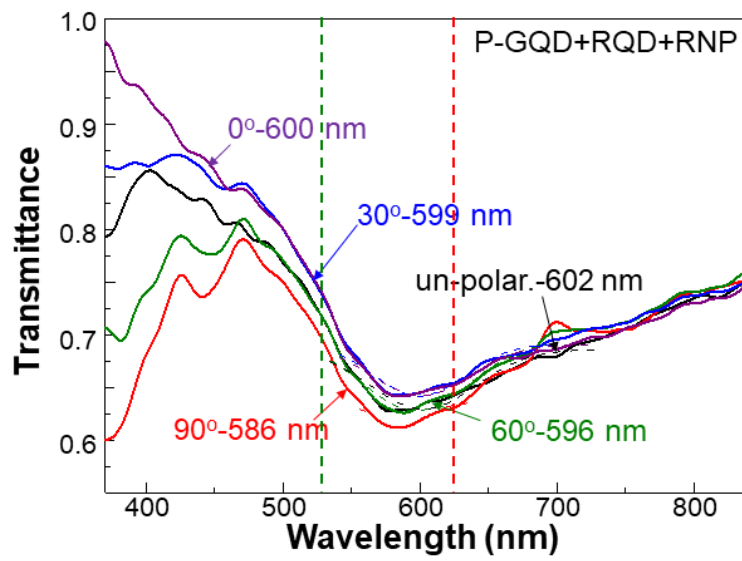


Fig 3.8 Results similar to those in Fig. 3.3 for sample P-GQD+RQD+RNP.

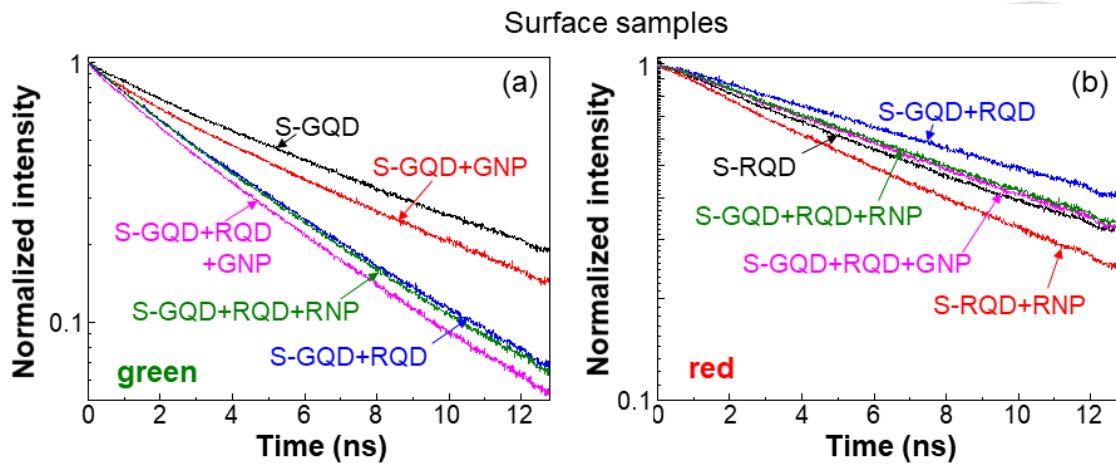


Fig 3.9 (a) and (b): Normalized PL decay profiles of the green and red components, respectively, for the surface samples.

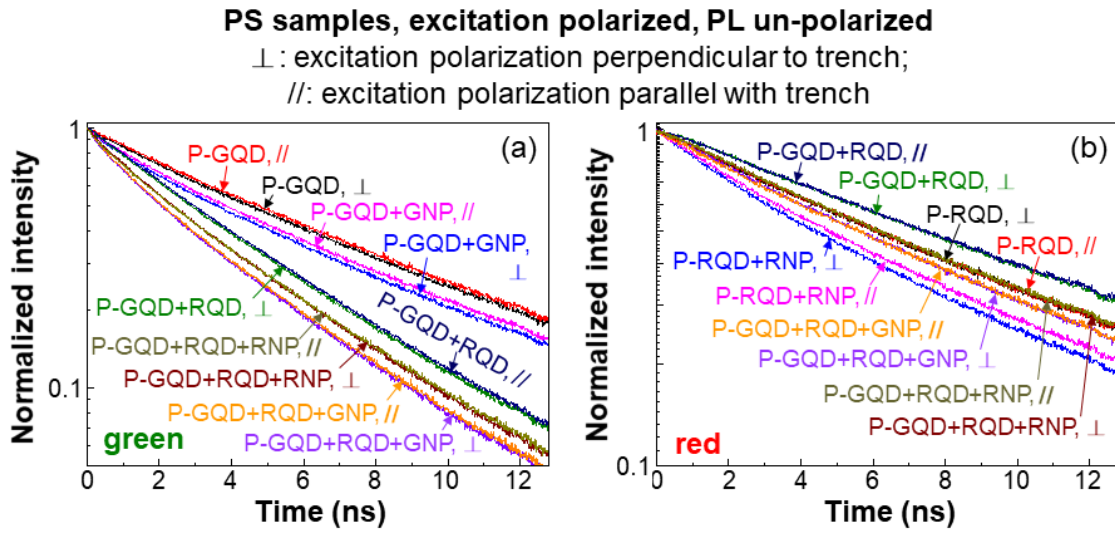


Fig 3.10 (a) and (b): Normalized PL decay profiles of the green and red components, respectively, for the PS samples under the conditions of polarized excitation, but un-polarized PL. The \perp and \parallel signs in the labels represent the excitation polarizations perpendicular to and parallel with the trench orientation.

PS samples, either excitation or PL polarized, 1

\perp : polarization perpendicular to trench; \parallel : polarization parallel with trench

First sign for excitation; second sign for PL

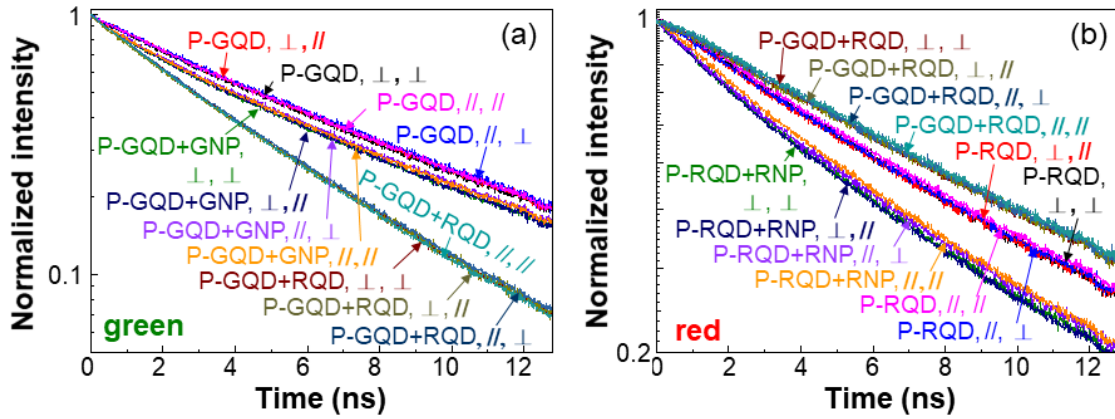


Fig 3.11 (a) and (b): Normalized PL decay profiles of the green and red components, respectively, for part of the PS samples under the conditions of polarized excitation and polarized PL. In the labels, the first (second) sign describes the excitation (PL) polarization.

PS samples, either excitation or PL polarized, 2

⊥ : polarization perpendicular to trench; //: polarization parallel with trench

First sign for excitation; second sign for PL

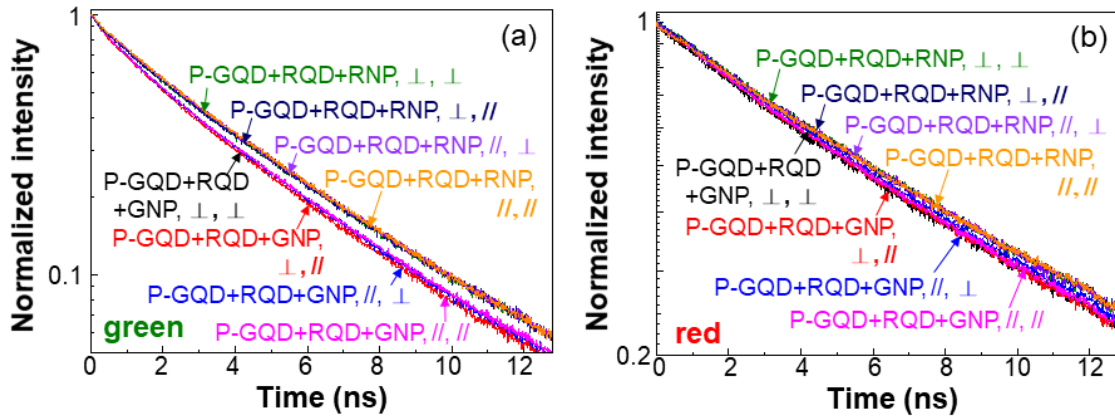


Fig 3.12 (a) and (b): Normalized PL decay profiles of the green and red components, respectively, for samples P-GQD+RQD+GNP and P-GQD+RQD+RNP under the conditions of polarized excitation and polarized PL.

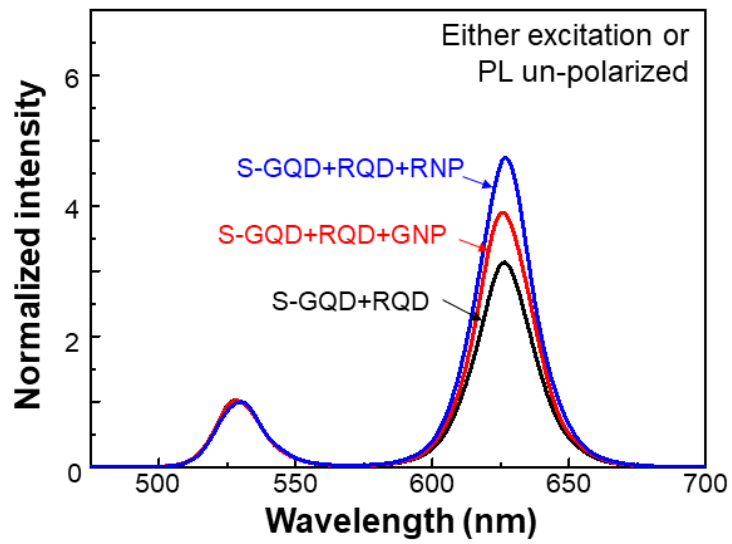


Fig 3.13 Normalized PL spectra of the three surface samples with both GQD and RQD.

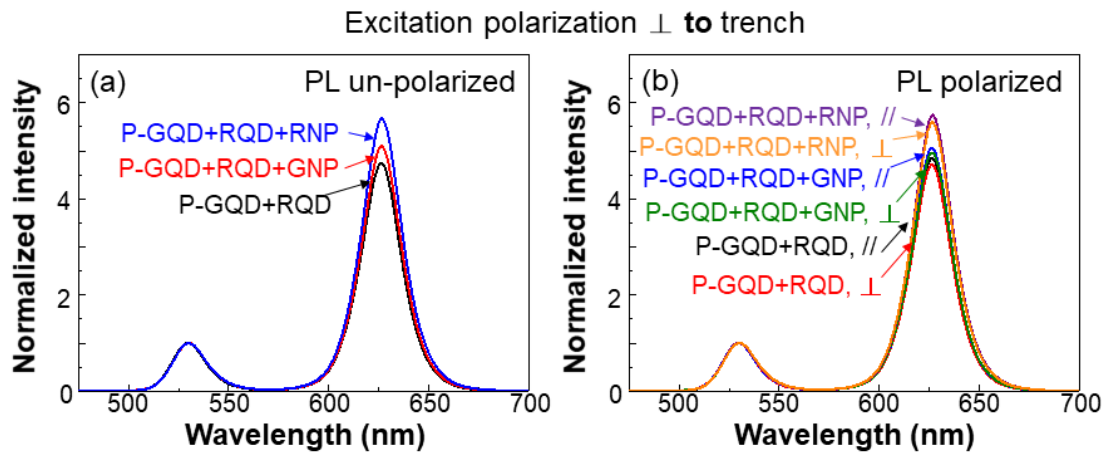


Fig 3.14 (a) and (b): Normalized PL spectra of the PS samples when the excitation polarization is perpendicular to trench orientation under the conditions of un-polarized and polarized PL, respectively.

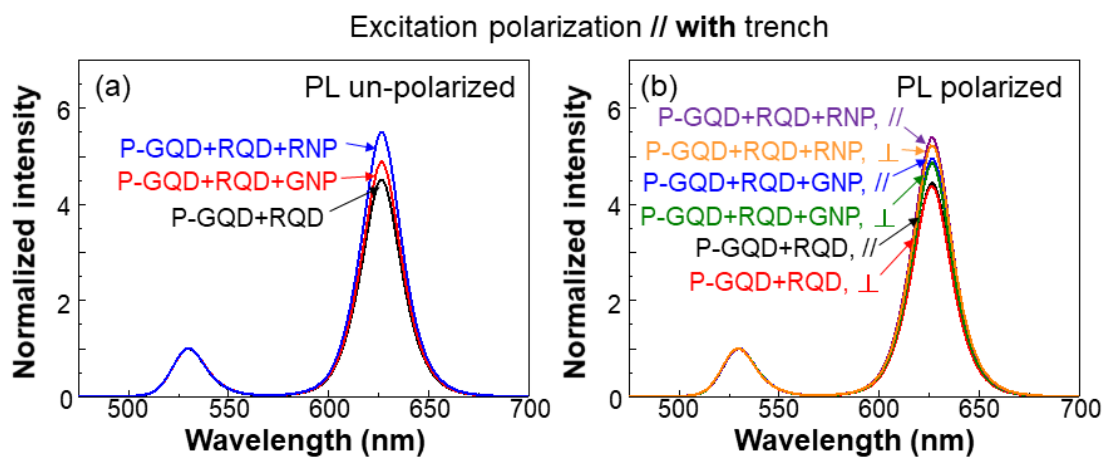


Fig 3.15 (a) and (b): Normalized PL spectra of the PS samples, similar to those in Figs. 3.14(a) and 3.14(b), respectively, when the excitation polarization is parallel with trench orientation.

Chapter 4 Discussions

4.1 Polarization dependent surface plasmon resonance

As shown in Figs. 3.3-3.8, when an Ag NP is inserted into an etched trench, the LSP resonance occurs at a shorter wavelength and is stronger when the polarization is perpendicular to the trench orientation. The stronger LSP resonance in this polarization is consistent with the theoretical prediction in the case of a spherical Ag NP. However, the shorter wavelength contradicts the prediction in the same case. If the Ag NP is spherical in geometry, the LSP resonance wavelength should be longer in this polarization. For RNP, this contradiction is attributed to its nano-disk geometry. In particular, for easily inserting into the trench, the nano-disk face must be parallel with the trench sidewalls. In this situation, the aforementioned perpendicular polarization is also perpendicular to the nano-disk face, leading to a shorter LSP resonance. Regarding the LSP resonance strength, the nanoscale-cavity effect in this direction can help in enhancing the LSP resonance. The anisotropic nanoscale-cavity effect is an important cause for the observed polarization dependent LSP resonance. For GNP, it is closer to a spherical geometry. However, its polarization dependent LSP resonance behavior in an etched trench is similar to that of RNP. The polarization dependent LSP resonance behavior of GNP deserves further investigation.

4.2 Polarization dependent quantum dot emission behaviors

The Purcell effect in the near field regime is quite different from that caused by far field. Inside a nanoscale cavity, the electromagnetic behavior produced by a dipole source is expected to differ from that of cavity resonance. Such a nanoscale-cavity effect is useful for enhancing the efficiencies of emission, SP coupling, and color conversion in a light-emitting device for illumination and display applications [7, 8, 15, 49-51]. In the current study, the nano-grating structure can produce a nanoscale-cavity effect when the polarization is perpendicular to the

oriented trench extension direction. Therefore, we would expect a higher QD emission efficiency, a stronger SP coupling, and a higher color conversion efficiency when polarization is perpendicular to the trench orientation. It is noted that color conversion relies on two factors, including FRET efficiency and acceptor emission efficiency. Although the observed FRET efficiency is not higher in the perpendicular polarization, the higher acceptor emission efficiency can help in producing a higher color conversion efficiency in this polarization, as shown in Table 3.4. The details of the polarization dependence in the fabricated samples deserve further investigation.

4.3 Accuracy of optical measurement

It is noted that the footprint of excitation laser onto a sample in either continuous or time-resolved PL measurement is larger than 300 micron. In other words, the excitation footprint is larger than the width of a stripe mesa. As mentioned above, in a mesa, all the ECE etched trenches are oriented in the same direction. However, between two neighboring mesas, there is a 5-micron separation region, in which no oriented trench structure exists. In this region, QDs and/or Ag NPs also exist. Therefore, the contribution of this region to the collected signal in an optical measurement can distort the polarization dependence of the measured results. To solve this problem, in designing the mesa pattern, we purposely minimize the width of the mesa separation region and maximize the width of a stripe mesa. Also, we need to consider the lateral range limitation in ECE for minimizing the ECE dividing band width [see Figs. 2.7(c) and 2.7(d)] such that the area of oriented etched trench can be maximized. Under the current experimental condition, by assuming that the ECE dividing band width is 100 nm, the width ratio of oriented etched trenches (the study target) over other structures is estimated to give 58.8 (299.9 micron over 5.1 micron). This large ratio guarantees the small inaccuracies in our optical measurements.

Chapter 5 Conclusions

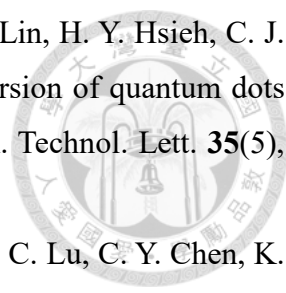
In summary, by well designing the epitaxial structure and the geometry of a stripe mesa array, subsurface oriented pores in a GaN layer could be formed through an ECE process. After removing the capping layer, surface oriented trenches of a fixed extension direction on the mesas could be implemented to form a deep grating of sub-100 nm in period without using any nano-lithography process. By drop-casting colloidal QDs and chemically synthesized Ag NPs onto the surface of such a sample, they could be naturally settled into the trenches for showing their polarization-dependent optical properties. Polarization-dependent SP resonance and coupling, FRET, and QD emission were studied based on the spectroscopy measurements of transmission, continuous PL and time-resolved PL. Generally speaking, when the excitation polarization was perpendicular to the trench orientation, QD emission and SP coupling were stronger. However, the FRET efficiency was lower. The overall color conversion efficiency was higher when the excitation polarization was perpendicular to the trench orientation.

References:

1. E. M. Purcell, H. C. Torrey, and R. V. Pound, "Resonance absorption by nuclear magnetic moments in a solid," *Phys. Rev.* **69**, 37-38 (1946).
2. D. Chen, H. Xiao, and J. Han, "Nanopores in GaN by electrochemical anodization in hydrofluoric acid formation and mechanism," *J. Appl. Phys.* **112**(6), 064303 (2012).
3. P. H. Griffin and R. A. Oliver, "Porous nitride semiconductors reviewed," *J. Phys. D: Appl. Phys.* **53**(38), 383002 (2020).
4. M. J. Schwab, D. Chen, J. Han, and L. D. Pfefferle, "Aligned mesopore arrays in GaN by anodic etching and photoelectrochemical surface etching," *J. Phys. Chem. C*, **117**(33), 16890-16895 (2013).
5. M. J. Schwab, J. Han, and L. D. Pfefferle, "Neutral anodic etching of GaN for vertical or crystallographic alignment," *Appl. Phys. Lett.* **106**(24), 241603 (2015).
6. W. J. Tseng, D. H. van Dorp, R. R. Lieten, P. M. Vereecken, and G. Borghs, "Anodic etching of n-GaN epilayer into porous GaN and its photoelectrochemical properties," *J. Phys. Chem. C* **118**(51), 29492-29498 (2014).
7. C. H. Chen, S. Y. Kuo, H. Y. Feng, Z. H. Li, S. Yang, S. H. Wu, H. Y. Hsieh, Y. S. Lin, Y. C. Lee, W. C. Chen, P. H. Wu, J. C. Chen, Y. Y. Huang, Y. J. Lu, Y. Kuo, C. F. Lin, and C. C. Yang, "Photon color conversion enhancement of colloidal quantum dots inserted into a subsurface laterally-extended GaN nano-porous structure in an InGaN/GaN quantum-well template," *Opt. Express* **31**(4), 6327-6341 (2023).
8. S. Yang, H. Y. Feng, Y. S. Lin, W. C. Chen, Y. Kuo, and C. C. Yang, "Effects of surface plasmon coupling on the color conversion from an InGaN/GaN quantum-well structure into colloidal quantum dots inserted into a nearby porous structure," *Nanomaterials* **13**(2), 328 (2023).
9. S. Chanyawadee, P. G. Lagoudakis, R. T. Harley, M. D. B. Charlton, D. V. Talapin, H. W. Huang, and C. H. Lin, "Increased color-conversion efficiency in hybrid light-emitting diodes utilizing non-radiative energy transfer," *Adv. Mater.* **22**(5), 602-606 (2010).
10. C. Krishnan, M. Brossard, K.-Y. Lee, J.-K. Huang, C.-H. Lin, H.-C. Kuo, M. D. B. Charlton, and P. G. Lagoudakis, "Hybrid photonic crystal light-emitting diode renders 123% color conversion effective quantum yield," *Optica* **3**(5), 503-509 (2016).
11. Z. Zhuang, X. Guo, B. Liu, F. Hu, Y. Li, T. Tao, J. Dai, T. Zhi, Z. Xie, P. Chen, D. Chen, H. Ge, X. Wang, M. Xiao, Y. Shi, Y. Zheng, and R. Zhang, "High color rendering index hybrid III-nitride/nanocrystals white light-emitting diodes," *Adv. Funct. Mater.* **26**(1), 36-

43 (2016).

12. M. Athanasiou, P. Papagiorgis, A. Manoli, C. Bernasconi, N. Poyiatzis, P.-M. Coulon, P. Shields, M. I. Bodnarchuk, M. V. Kovalenko, T. Wang, and G. Itskos, "InGaN nanohole arrays coated by lead halide perovskite nanocrystals for solid-state lighting," *ACS Appl. Nano Mater.* **3**(3), 2167-2175 (2020).
13. R. Wan, G. Li, X. Gao, Z. Liu, J. Li, X. Yi, N. Chi, and L. Wang, "Nanohole array structured GaN-based white LEDs with improved modulation bandwidth via plasmon resonance and non-radiative energy transfer," *Photon. Res.* **9**(7), 1213-1217 (2021).
14. Z. Du, D. Li, W. Guo, F. Xiong, P. Tang, X. Zhou, Y. Zhang, T. Guo, Q. Yan, and J. Sun, "Quantum dot color conversion efficiency enhancement in micro-light-emitting diodes by non-radiative energy transfer," *IEEE Electron Dev. Lett.* **42**(8), 1184-1187 (2021).
15. Y. Y. Huang, Z. H. Li, Y. C. Lai, J. C. Chen, S. H. Wu, S. Yang, Y. Kuo, C. C. Yang, T. C. Hsu, and C. L. Lee, "Nanoscale-cavity enhancement of color conversion with colloidal quantum dots embedded in the surface nano-holes of a blue-emitting light-emitting diode," *Opt. Express* **30**(17), 31322-31335 (2022).
16. T. Förster, "Energy transport and fluorescence," *Naturwissenschaften* **33**, 166-175 (1946).
17. S. Chanyawadee, P. G. Lagoudakis, R. T. Harley, M. D. B. Charlton, D. V. Talapin, H. W. Huang, and C. H. Lin, "Increased color-conversion efficiency in hybrid light-emitting diodes utilizing non-radiative energy transfer," *Adv. Mater.* **22**(5), 602-606 (2010).
18. H. V. Demira, S. Nizamoglu, T. Erdemb, E. Mutluguna, N. Gaponik, and A. Eychmuller, "Quantum dot integrated LEDs using photonic and excitonic color conversion," *Nano Today* **6**(6), 632-647 (2011).
19. F. Zhang, J. Liu, G. You, C. Zhang, S. E. Mohny, M. J. Park, J. S. Kwak, Y. Wang, D. D. Koleske, and J. Xu, "Nonradiative energy transfer between colloidal quantum dot-phosphors and nanopillar nitride LEDs," *Opt. Express* **20**(S2), A333-A339 (2012).
20. C. C. Ni, S. Y. Kuo, Z. H. Li, S. H. Wu, R. N. Wu, C. Y. Chen, and C. C. Yang, "Förster resonance energy transfer in surface plasmon coupled color conversion processes of colloidal quantum dots," *Opt. Express* **29**(3), 4067-4081 (2021).
21. Y. P. Chen, C. C. Ni, R. N. Wu, S. Y. Kuo, Y. C. Su, Y. Y. Huang, J. W. Chen, Y. C. Hsu, S. H. Wu, C. Y. Chen, P. H. Wu, Y. W. Kiang, and C. C. Yang, "Combined effects of surface plasmon coupling and Förster resonance energy transfer on the light color conversion behaviors of colloidal quantum dots on an InGaN/GaN quantum-well nanodisk structure," *Nanotechnology* **32**(13), 135206 (2021).

- 
22. S. Yang, Y. C. Lai, H. Y. Feng, Y. C. Lee, Z. H. Li, S. H. Wu, Y. S. Lin, H. Y. Hsieh, C. J. Chu, W. C. Chen, Y. Kuo, and C. C. Yang, "Enhanced color conversion of quantum dots located in the hot spot of surface plasmon coupling," *IEEE Photon. Technol. Lett.* **35**(5), 273-276 (2023).
23. Y. Kuo, S. Y. Ting, C. H. Liao, J. J. Huang, C. Y. Chen, C. Hsieh, Y. C. Lu, C. Y. Chen, K. C. Shen, C. F. Lu, D. M. Yeh, J. Y. Wang, W. H. Chuang, Y. W. Kiang, and C. C. Yang, "Surface plasmon coupling with radiating dipole for enhancing the emission efficiency of a light-emitting diode," *Opt. Express* **19**(14), A914-A929 (2011).
24. Y. Kuo, W. Y. Chang, C. H. Lin, C. C. Yang, and Y. W. Kiang, "Evaluating the blue-shift behaviors of the surface plasmon coupling of an embedded light emitter with a surface Ag nanoparticle by adding a dielectric interlayer or coating," *Opt. Express* **23**(24), 30709-30720 (2015).
25. C. J. Cai, Y. T. Wang, C. C. Ni, R. N. Wu, C. Y. Chen, Y. W. Kiang, and C. C. Yang, "Emission behaviors of colloidal quantum dots linked onto synthesized metal nanoparticles," *Nanotechnology* **31**(9), 095201 (2020)
26. Y. T. Wang, C. W. Liu, P. Y. Chen, R. N. Wu, C. C. Ni, C. J. Cai, Y. W. Kiang, and C. C. Yang, "Color conversion efficiency enhancement of colloidal quantum dot through its linkage with synthesized metal nanoparticle on a blue light-emitting diode," *Opt. Lett.* **44**(23), 5691-5694 (2019).
27. W. Y. Chang, Y. Kuo, Y. W. Kiang, and C. C. Yang, "Simulation study on light color conversion enhancement through surface plasmon coupling," *Opt. Express* **27**(12), A629-A642 (2019).
28. C. H. Lin, H. C. Chiang, Y. T. Wang, Y. F. Yao, C. C. Chen, W. F. Tse, R. N. Wu, W. Y. Chang, Y. Kuo, Y. W. Kiang, and C. C. Yang, "Efficiency enhancement of light color conversion through surface plasmon coupling," *Opt. Express* **26**(18), 23629-23640 (2018).
29. C. Y. Chen, C. C. Ni, R. N. Wu, S. Y. Kuo, C. H. Li, Y. W. Kiang, and C. C. Yang, "Surface plasmon coupling effects on the Förster resonance energy transfer from quantum dot into rhodamine 6G," *Nanotechnology* **32**(29), 295202 (2021).
30. W. J. Hsu, K. T. Chen, W. C. Huang, C. J. Wu, J. J. Dai, S. H. Chen, and C. F. Lin, "InGaN light emitting diodes with a nanopipe layer formed from the GaN epitaxial layer." *Opt. Express* **24**(11), 11601-11610 (2016).
31. Y. Li, C. Wang, Y. Zhang, P. Hu, S. Zhang, M. Du, X. Su, Q. Li, and F. Yun, "Analysis of TM/TE mode enhancement and droop reduction by a nanoporous n-AlGaIn underlayer in

- a 290 nm UV-LED,” *Photon. Res.* **8**(6), 806-811 (2020).
32. C. B. Soh, C. B. Tay, R. J. N. Tan, A. P. Vajpeyi, I. P. Seetoh, K. K. Ansah-Antwi, and S. J. Chua, “Nanopore morphology in porous GaN template and its effect on the LEDs emission,” *J. Phys. D: Appl. Phys.* **46**(36), 365102 (2013).
33. C. Wurm, H. Collins, N. Hatui, W. Li, S. Pasayat, R. Hamwey, K. Sun, I. Sayed, K. Khan, E. Ahmadi, S. Keller, and U. Mishra, “Demonstration of device-quality 60% relaxed In_{0.2}Ga_{0.8}N on porous GaN pseudo-substrates grown by PAMBE,” *J. Appl. Phys.* **131**(1), 015701 (2022).
34. S. S. Pasayat, C. Gupta, M. S. Wong, R. Ley, M. J. Gordon, S. P. DenBaars, S. Nakamura, S. Keller, and U. Mishra, “Demonstration of ultra-small (<10 μm) 632 nm red InGaN micro-LEDs with useful on-wafer external quantum efficiency (>0.2%) for mini-displays,” *Appl. Phys. Express* **14**(1), 011004 (2021).
35. S. Huang, Y. Zhang, B. Leung, G. Yuan, G. Wang, H. Jiang, Y. Fan, Q. Sun, J. Wang, K. Xu, and J. Han, “Mechanical properties of nanoporous GaN and its application for separation and transfer of GaN thin films,” *ACS Appl. Mater. Interfaces* **5**(21), 11074-11079 (2013).
36. Y. Zhang, Q. Sun, B. Leung, J. Simon, M. L. Lee, and J. Han, “The fabrication of large-area, free-standing GaN by a novel nanoetching process,” *Nanotechnology* **22**(4), 045603 (2011).
37. J. H. Kang, M. Ebaid, J. K. Lee, T. Jeong, and S. W. Ryu, “Fabrication of vertical light emitting diode based on thermal deformation of nanoporous GaN and removable mechanical supporter,” *ACS Appl. Mater. Interfaces* **6**(11), 8683-8687 (2014).
38. C. Zhang, S. H. Park, D. Chen, D. W. Lin, W. Xiong, H. C. Kuo, C. F. Lin, H. Cao, and J. Han, “Mesoporous GaN for photonic engineering highly reflective GaN mirrors as an example,” *ACS Photon.* **2**(7), 980-986 (2015).
39. C. F. Lin, Y. T. Zhang, C. J. Wang, Y. Y. Chen, G. Y. Shiu, Y. Ke, and J. Han, “InGaN resonant microcavity with n⁺-porous-GaN/p⁺-GaN tunneling junction,” *IEEE Electron Dev. Lett.* **42**(11), 1631-1633 (2021).
40. A. Najar, M. Gerland, and M. Jouiad, “Porosity-induced relaxation of strains in GaN layers studied by means of microindentation and optical spectroscopy,” *J. Appl. Phys.* **111**(9), 093513 (2012).
41. S. S. Pasayat, N. Hatui, W. Li, C. Gupta, S. Nakamura, S. P. Denbaars, S. Keller, and U. Mishra, “Method of growing elastically relaxed crack-free AlGaIn on GaN as substrates for

- ultra-wide bandgap devices using porous GaN,” *Appl. Phys. Lett.* **117**(6), 062102 (2020).
42. S. S. Pasayat, C. Gupta, M. S. Wong, Y. Wang, S. Nakamura, S. P. Denbaars, S. Keller, and U. Mishra, “Growth of strain-relaxed InGaN on micrometersized patterned compliant GaN pseudo-substrates,” *Appl. Phys. Lett.* **116**(11), 111101 (2020).
43. J. H. Kang, B. Li, T. Zhao, M. Ali Johar, C. C. Lin, Y. H. Fang, W. H. Kuo, K. L. Liang, S. Hu, S. W. Ryu, and J. Han, “RGB arrays for micro-light-emitting diode applications using nanoporous GaN embedded with quantum dots,” *ACS Appl. Mater. Interfaces* **12**(27), 30890-30895 (2020).
44. R. Anderson, D. Cohen, H. Zhang, E. Trageser, N. Palmquist, S. Nakamura, and S. DenBaars, “Nano-porous GaN cladding and scattering loss in edge emitting laser diodes,” *Opt. Express* **30**(2), 2759-2767 (2022).
45. Y. Ke, C. J. Wang, G. Y. Shiu, Y. Y. Chen, Y. S. Lin, H. Chen, J. Han, and C. F. Lin, “Polarization properties of InGaN vertical-cavity surface-emitting laser with pipe distributed Bragg reflector,” *IEEE Transact. Electron Dev.* **69**(1), 201-204 (2022).
46. R. T. Elafandy, J. H. Kang, C. Mi, T. K. Kim, J. S. Kwak, and J. Han, “Study and application of birefringent nanoporous GaN in the polarization control of blue vertical-cavity surface-emitting lasers,” *ACS Photon.* **8**(4), 1041-1047 (2021).
47. C. A. J. Lin, R. A. Sperling, J. K. Li, T. A. Yang, P. Y. Li, M. Zanella, W. H. Chang, and W. J. Parak, “Design of an amphiphilic polymer for nanoparticle coating and functionalization,” *Small* **4**(3), 334-341 (2008).
48. P. Ghenuche, M. Mivelle, J. de Torres, S. B. Moparthi, H. Rigneault, N. F. V. Hulst, M. F. G. Parajó, and J. Wenger, “Matching nanoantenna field confinement to FRET distances enhances Förster energy transfer rates,” *Nano Lett.* **15**(9), 6193-6201 (2015).
49. Y. Kuo, Y. J. Lu, C. Y. Shih, and C. C. Yang, “Simulation study on the enhancement of resonance energy transfer through surface plasmon coupling in a GaN porous structure,” *Opt. Express* **29**(26), 43182-43192 (2021).
50. Y. C. Lai, S. Yang, H. Y. Feng, Y. C. Lee, Z. H. Li, S. H. Wu, Y. S. Lin, H. Y. Hsieh, C. J. Chu, W. C. Chen, Y. Y. Huang, Y. Kuo, and C. C. Yang, “Surface plasmon coupling effects on the photon color conversion behaviors of colloidal quantum dots in a GaN nanoscale hole with a nearby quantum-well structure,” *Opt. Express* **31**(10), 16010-16024 (2023).
51. Y. Kuo and C. C. Yang, “Theoretical/numerical studies of the nanoscale-cavity effects on dipole emission, Förster resonance energy transfer and surface plasmon coupling,” to appear in *Plasmonics*.